

Axion forces in axion backgrounds

Yuval Grossman,^a Bingrong Yu,^a Siyu Zhou^{a,b}

^a*Department of Physics, LEPP, Cornell University, Ithaca, NY 14853, USA*

^b*University of Science and Technology of China, Hefei, Anhui 230026, China*

E-mail: yg73@cornell.edu, bingrong.yu@cornell.edu, sz682@cornell.edu

ABSTRACT: Axions can naturally be very light due to the protection of (approximate) shift symmetry. Because of the pseudoscalar nature, the long-range force mediated by the axion at the tree level is spin dependent, which cannot lead to observable effects between two unpolarized macroscopic objects. At the one-loop level, however, the exchange of two axions does mediate a spin-independent force. This force is coherently enhanced when there exists an axion background. In this work, we study the two-axion exchange force in a generic axion background. We find that the breaking of the axion shift symmetry plays a crucial role in determining this force. The background-induced axion force V_{bkg} vanishes in the shift-symmetry restoration limit. The shift symmetry can be broken either explicitly by non-perturbative effects or effectively by the axion background. When the shift symmetry is broken, V_{bkg} scales as $1/r$ and could be further enhanced by a large occupation number of the background axions. We investigate possible probes on this using fifth-force search and atomic spectroscopy experiments. Using existing data, we find that the background-induced axion force imposes constraints on axion couplings and masses that are stronger than previously available limits in certain regions of parameter space.

Contents

| | | |
|----------|---|-----------|
| 1 | Introduction | 1 |
| 2 | The formalism of background-induced axion forces | 3 |
| 2.1 | Shift-invariant axion interaction | 4 |
| 2.1.1 | Calculation of the amplitude | 5 |
| 2.1.2 | Order parameters | 9 |
| 2.1.3 | Decoherence factor | 11 |
| 2.1.4 | Further discussions | 12 |
| 2.2 | Breaking of the shift symmetry | 12 |
| 2.2.1 | Quadratic coupling from non-perturbative effects | 12 |
| 2.2.2 | Effective shift-symmetry breaking from axion backgrounds | 15 |
| 2.3 | Summary | 16 |
| 3 | Typical axion backgrounds | 16 |
| 3.1 | Maxwell-Boltzmann distribution | 17 |
| 3.2 | Bose-Einstein distribution | 17 |
| 3.3 | Relativistic axion flux | 19 |
| 4 | Experimental probes of the axion forces | 20 |
| 4.1 | Axion dark matter | 21 |
| 4.1.1 | Coherent limit | 21 |
| 4.1.2 | Decoherence effect | 23 |
| 4.1.3 | Fifth-force bounds | 27 |
| 4.2 | Solar axion flux | 30 |
| 4.3 | Atomic spectroscopy | 31 |
| 5 | Comparison with the literature | 34 |
| 6 | Conclusions | 35 |
| A | Axion forces at the tree level | 36 |
| B | Pseudoscalar basis versus derivative basis | 38 |
| C | Compton scattering of axions | 39 |
| D | Derivation of V_{bkg} from coherent scattering | 41 |
| E | Relevant integrals | 43 |
| E.1 | Relativistic corrections | 45 |

| | | |
|----------|---|-----------|
| F | Decoherence effects on the axion force | 47 |
| F.1 | Point-like object | 47 |
| F.2 | Finite-size object | 48 |
| G | Axion forces from solar axion flux | 49 |

1 Introduction

The axion appears as a pseudo-Nambu-Goldstone boson (pNGB) of a spontaneously broken $U(1)$ global symmetry [1, 2]. It is well motivated both in particle physics to solve the strong CP problem [3, 4] and in cosmology to serve as the candidate of cold dark matter (DM) [5–8], see [9, 10] for recent reviews of axion physics and its cosmology. As a generic feature of pNGB, the axion mass is protected by the shift symmetry. Nonzero axion mass originates from non-perturbative instanton effects that lead to

$$m_a \sim \frac{\mu_0^2}{f_a}, \quad (1.1)$$

where μ_0 is the scale of the non-perturbative effects that explicitly break the shift symmetry (for the QCD axion, $\mu_0 \sim \Lambda_{\text{QCD}} \approx 200$ MeV), and f_a (known as the axion decay constant) is the scale of the spontaneous $U(1)$ symmetry breaking, which characterizes the (inverse) axion coupling strength to the ordinary matter. We learn from Eq. (1.1) that m_a can naturally be small if $\mu_0 \ll f_a$, as is usually assumed in axion models. Moreover, the radiative corrections to the axion mass are all suppressed by high powers of f_a , thus making the axion mass protected from quantum corrections.

Given that the axion can naturally be very light from the theoretical point of view, one may expect a long-range force between macroscopic objects mediated by axions. This “axion force” already exists at the tree level, i.e., by the exchange of one axion [11, 12]. In this work, we consider only the CP-conserving axion interactions. Due to the pseudoscalar nature of the axion couplings, the one-axion force between two fermions is spin-dependent and only results in the dipole-dipole interaction:

$$V_a(\mathbf{r}) \sim \frac{1}{f_a^2} (\boldsymbol{\sigma}_1 \cdot \nabla) (\boldsymbol{\sigma}_2 \cdot \nabla) \frac{e^{-m_a r}}{4\pi r}, \quad (1.2)$$

where $\boldsymbol{\sigma}_1$ and $\boldsymbol{\sigma}_2$ are the spin vectors of the two external fermions. Note that since we do not include CP-violating axion couplings such as $a\bar{\psi}\psi$, there are no monopole-monopole or monopole-dipole interactions at the tree level. (For the searches of the axion force when there exist CP-violating interactions, see [13–19].)

In the massless axion limit, Eq. (1.2) scales as $V_a \sim 1/(f_a^2 r^3)$. However, this force vanishes for unpolarized sources as the spin prefactor in Eq. (1.2) averages to zero (see App. A). As

a result, it cannot lead to observable effects in the traditional fifth-force experiments with unpolarized sources. This is in contrast with the CP-even scalar, where in the latter case the scalar-mediated force at the tree level is spin-independent and the fifth-force searches can probe very small scalar couplings in the small mass region [20, 21]. The spin-dependent axion force in Eq. (1.2) can only be tested when the source has some net polarization; see [22–26] for the detection of spin-dependent interactions with polarized sources. However, one should note that the dipole-dipole axion force scales as $1/r^3$, which is much smaller than the $1/r$ Yukawa force at long distances. As a result, the bounds from fifth-force searches on the axion interaction via Eq. (1.2) are much weaker than those of a CP-even scalar.

The spin-independent axion force starts to appear at the one-loop level by the exchange of two axions, which is a quantum effect. This two-axion force was first calculated in [27, 28] (see also [29]), in which they obtained $V_{2a} \sim 1/(f_a^4 r^5)$ for massless axions. Although this effect is coherent over macroscopic objects, it is heavily suppressed due to the r^{-5} factor.

Recently, it was pointed out in [30, 31] that breaking the axion shift symmetry can enhance the two-axion force. More specifically, for the QCD axion, non-perturbative effect below the confinement scale induces a shift-symmetry-breaking coupling of the form $\mu a^2 \bar{N} N / f_a^2$ between axions and nucleons, where $\mu \sim \mathcal{O}(10)$ MeV. Such a coupling leads to an axion force scaling as $V_{2a} \sim \mu^2 / (f_a^4 r^3)$, which dominates over the one in the shift-invariant limit. Combined with the fifth-force searches at the laboratory length scale, it gives a constraint on the axion coupling $f_a \gtrsim 10$ GeV [30].

An important feature of the two-axion force is that it can be influenced by an axion background. In vacuum, the interaction between test particles is mediated by two virtual axions, both of which are generated from quantum fluctuations. However, when there exists an axion background, the interaction can also be mediated by the scattering between test particles and background axions. Intuitively, it is equivalent to putting one of the axion propagators on-shell. Such an effect is coherent over background axions if their de Broglie wavelength is larger than the distance between the test particles. The background-induced axion force may change the r -dependence of its vacuum counterpart and lead to dominant observable effects.

The background effect is a generic feature of quantum forces, which is essentially a result of coherent scattering. In recent years, there has been growing interest in studying this phenomenon, including the detection of the neutrino-mediated force in various neutrino backgrounds in the Standard Model framework [32–34] and the applications of background effects in the search for light DM [35–50]; for earlier studies on this topic, see [51–55]. In particular, recent work [42, 43] calculated the DM background-induced forces when the DM particle couples quadratically to fermions and investigated their implications in fifth-force search experiments.

Various axion background profiles can remain today based on well-motivated particle physics and cosmological models. A huge occupation number of the background axions is expected to exist as relics if the axions make up the cold DM [8]. Axions can also be copiously produced in the early universe via different mechanisms and comprise the cosmic axion

background at present day [56]. Moreover, an energetic axion flux with energies of order keV can be produced from the Sun through axion coupling to photons [57].

Since the axion background may significantly change the axion force and affect the detection of axions, in this work, we aim to perform a systematic study on the axion forces in various axion backgrounds. Our main findings are:

- The magnitude of the background-induced axion force V_{bkg} is determined by the degree of shift symmetry breaking in the theory. In particular, in the shift-symmetry restoration limit, V_{bkg} vanishes at the leading order of the non-relativistic approximation of the external particles.
- The existence of an axion background can effectively violate the shift symmetry, which enhances V_{bkg} if the energy scale of the background is larger than the axion mass.
- V_{bkg} has a different scaling behavior from its vacuum counterpart V_{2a} . In particular, unlike V_{2a} , V_{bkg} is generically not exponentially suppressed at long distances $r \gg 1/m_a$.
- In the coherent region ($r \ll \lambda_{\text{dB}}$), V_{bkg} has a generic scaling behavior $V_{\text{bkg}} \sim n_a/r$ that is independent of the details of backgrounds, where λ_{dB} and n_a are the typical de Broglie wavelength and the number density of background axions, respectively.

Given the above features, we find that V_{bkg} can dominate over V_{2a} in a large region of the parameter space of axion mass and couplings.

This paper is organized as follows. In Sec. 2, we derive the general formalism of the axion force in the existence of an arbitrary axion background, with both shift-invariant and breaking interactions taken into account. Then we apply it to studying the axion forces in three typical axion backgrounds in Sec. 3. We discuss the specific experimental probes of the axion forces in Sec. 4. A comparison between our results and the existing literature is provided in Sec. 5 and our main conclusion is summarized in Sec. 6. Necessary technical details are provided in several appendices.

2 The formalism of background-induced axion forces

In this section, we derive the general formulae of the two-axion-exchange force in an arbitrary axion background. We first focus on the scenario where the axion interactions are subject to shift-invariant symmetry but still allow for a finite axion mass. We show that V_{bkg} vanishes in the shift-invariant limit, regardless of the details of the background. Then we introduce sources of shift-symmetry breaking and calculate their effects on the axion force.

As we show below, the background-induced axion force between two fermions ψ_1 and ψ_2 has a generic form:

$$\boxed{V_{\text{bkg}}(r) \sim \frac{n_a}{4\pi r} \times \frac{m_1 m_2}{f_a^4} \times \frac{\text{order parameter}}{\text{background scale}} \times \text{decoherence factor} .} \quad (2.1)$$

In this expression,

- n_a is the number density of background axions;
- m_i is the mass of ψ_i ;
- the “order parameter” is a dimensionless quantity (normalized by the fermion mass) that characterizes the magnitude of shift-symmetry breaking in a theory, which tends to zero in the shift-invariant limit;
- the “background scale” is the typical energy scale of the axion background; it is reduced to the axion mass for non-relativistic axion backgrounds (such as the axion cold DM);
- the dimensionless “decoherence factor” describes the deviation of the axion force from a $1/r$ potential and can never exceed 1. For $r \gtrsim \lambda_{\text{dB}}$, V_{bkg} is more suppressed than $1/r$ due to the decoherence effect, while in the coherent limit $r \ll \lambda_{\text{dB}}$, the decoherence factor is reduced to 1 regardless of the details of the background.

In the following parts of this section, we discuss each term in Eq. (2.1) with more details.

2.1 Shift-invariant axion interaction

We start from the effective interaction between the axion, a , and a fermion, ψ :

$$\mathcal{L}_{\text{eff}} = \frac{1}{2} (\partial_\mu a) (\partial^\mu a) - \frac{1}{2} m_a^2 a^2 + \bar{\psi} (i\not{\partial} - m_\psi) \psi + \mathcal{L}_{\text{int}} . \quad (2.2)$$

The axion-fermion interaction term \mathcal{L}_{int} can be expressed in two equivalent forms (see App. B for details). In the *derivative basis*, the interaction term is written as

$$\mathcal{L}_{\text{int}}^{\text{d}} = \frac{c_\psi}{2} \frac{\partial_\mu a}{f_a} \bar{\psi} \gamma^\mu \gamma_5 \psi . \quad (2.3)$$

which has an explicit shift invariance: $a \rightarrow a + \text{constant}$. Equivalently, one can work it to the *pseudoscalar basis*:

$$\mathcal{L}_{\text{int}}^{\text{p}} = -i c_\psi m_\psi \frac{a}{f_a} \bar{\psi} \gamma_5 \psi + \frac{1}{2} c_\psi^2 m_\psi \frac{a^2}{f_a^2} \bar{\psi} \psi + \mathcal{O} \left(\frac{a^3}{f_a^3} \right) . \quad (2.4)$$

In Eq. (2.4), the shift invariance is kept up to $\mathcal{O}(1/f_a^2)$. Since we are interested in the two-axion effect in this work, it is sufficient to neglect the $\mathcal{O}(1/f_a^3)$ terms in the pseudoscalar basis.

The axion mass in Eq. (2.2) is the only term that breaks shift symmetry; it may come from unspecific nonperturbative effects at high-energy scales. In the following discussion we treat m_a as a free parameter for the purpose of generality.

At the tree-level, the derivative coupling in Eq. (2.3) induces an axion force between two fermions that is spin-dependent (see App. A). We are interested in the spin-independent axion

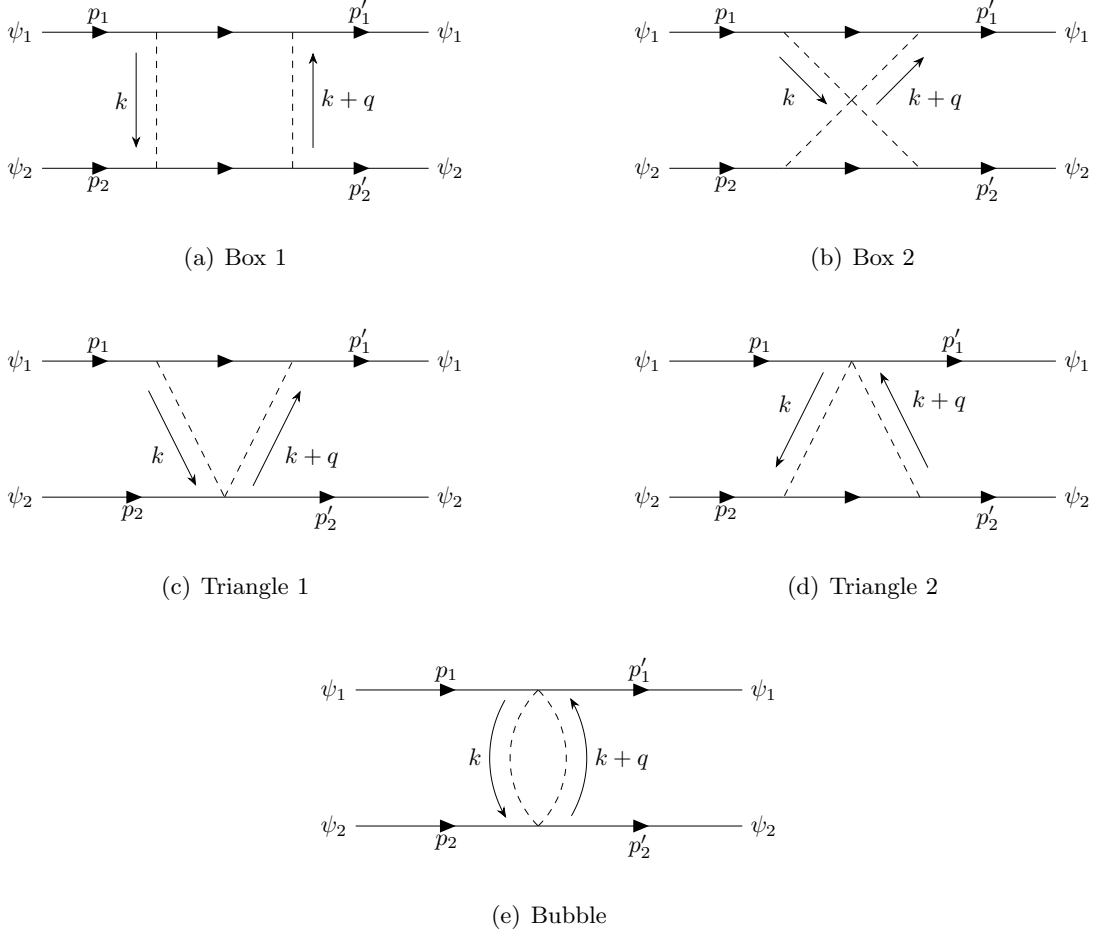


Figure 1. Feynman diagrams of two-axion exchange between two fermions ψ_1 and ψ_2 . Each of them can be affected by an axion background.

force, which starts to appear at the one-loop level (see Fig. 1). Note that in the derivative basis there is only linear axion coupling, so only the two box diagrams in Fig. 1 contribute, while in the pseudoscalar basis all five diagrams in Fig. 1 are relevant because there are both linear and quadratic couplings. However, the physical observable should not be affected by the basis we choose.

2.1.1 Calculation of the amplitude

To extract the axion force, one needs to calculate the amplitude of the elastic scattering $\psi_1(p_1) + \psi_2(p_2) \rightarrow \psi_1(p'_1) + \psi_2(p'_2)$ mediated by two axions with a momentum transfer $q = p'_1 - p_1 = p_2 - p'_2$. The effective potential mediated by axions is given by the Fourier transform

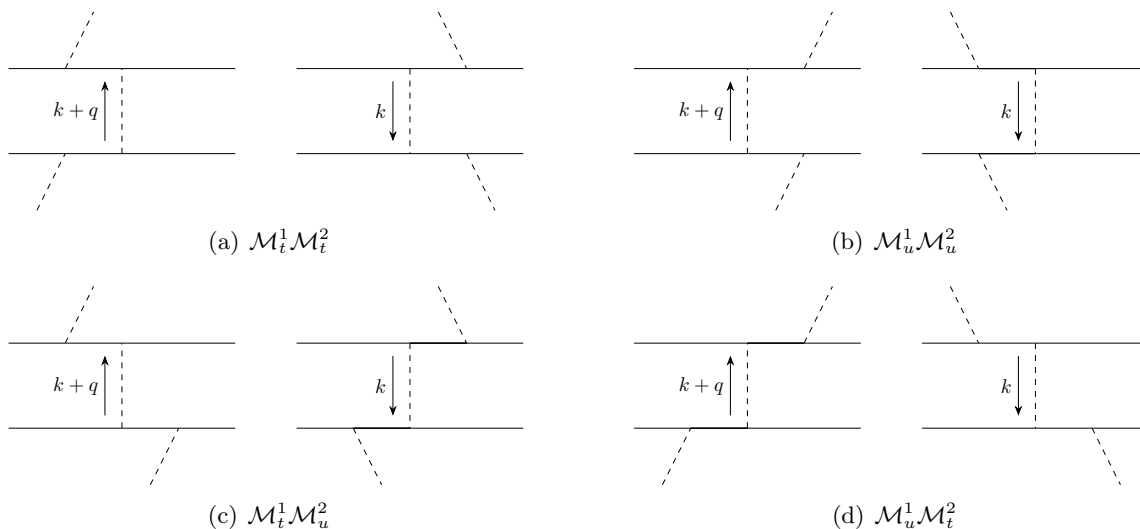


Figure 2. Effective box diagrams in the medium of axions that contribute to the background-induced axion force through coherent scattering. The four diagrams in the first line correspond to the “Box 1” diagram in Fig. 1, while those in the second line correspond to the “Box 2” diagram in Fig. 1. See App. D for detailed calculations.

of the scattering amplitude in the non-relativistic (NR) limit,

$$V(\mathbf{r}) = -\frac{1}{4m_1 m_2} \int \frac{d^3 \mathbf{q}}{(2\pi)^3} e^{i\mathbf{q}\cdot\mathbf{r}} \mathcal{M}_{\text{NR}}(\mathbf{q}). \quad (2.5)$$

In the NR limit, $q^\mu \approx (0, \mathbf{q})$, $4m_1 m_2$ is the normalization factor, and \mathcal{M}_{NR} denotes the scattering amplitude in the NR limit. The scattering amplitude includes contributions from the relevant diagrams in Fig. 1, which can be calculated using quantum field theories. For each of the diagrams, as we show in a while, the amplitude can be decomposed into the production of two tree-level Compton scattering amplitudes.

When there exists an axion background, the interaction can also be mediated by coherent scattering between ψ_i and on-shell background axions (see Fig. 2). To include the background effect, one can replace the vacuum axion propagator with the modified propagator:

$$D_{\text{mod}}(k) = \frac{i}{k^2 - m_a^2} + 2\pi\delta(k^2 - m_a^2) \Theta(k^0) f(\mathbf{k}) \equiv D_{\text{vac}}(k) + D_{\text{bkg}}(k), \quad (2.6)$$

where Θ is the step function and $f(\mathbf{k})$ is the phase-space distribution of background axions, normalized as

$$n_a = \int \frac{d^3 \mathbf{k}}{(2\pi)^3} f(\mathbf{k}). \quad (2.7)$$

The modified propagator in Eq. (2.6) contains two pieces: the first part is the axion

propagator in vacuum; the second part comes from the background correction, where the existence of δ -function implies that the background axions are on-shell. In addition, D_{bkg} is proportional to the phase-space number density, indicating that the background correction is a coherent effect, i.e., it is proportional to the axion number density at the amplitude level. The formalism in Eq. (2.6) has been widely used in the literature to calculate the background corrections in various cases [32–34, 43, 51–53, 55, 58]. It provides a compact and model-independent way to parametrize the background effect. More specifically, for each of the diagram in Fig. 1,

- when both axion propagators take D_{vac} , it gives the two-axion force in vacuum V_{2a} ;
- when one of the propagators takes D_{vac} and the other takes D_{bkg} , it gives the background-induced axion force V_{bkg} ;
- when both propagators take D_{bkg} , it does not contribute to the interaction between ψ_1 and ψ_2 .

We emphasize that Eq. (2.6) is essentially a result of coherent scattering between ψ_i and the background axions, as shown in Fig. 2. As a result, its validity does *not* require the background axions to be in thermal equilibrium. In App. D, we show how to derive the same result of the axion force using coherent scattering without assuming Eq. (2.6).

With the modified propagator in hand, we proceed to calculate the scattering amplitude in Eq. (2.5). For the relevant diagrams in Fig. 1, the total amplitude is given by

$$i\mathcal{M}_{\text{tot}} = \int \frac{d^4k}{(2\pi)^4} \int \frac{d^4k'}{(2\pi)^4} (2\pi)^4 \delta^{(4)}(q+k-k') D_{\text{mod}}(k) D_{\text{mod}}(k') \\ \times i\mathcal{M}_C(p_1, p'_1; -k, -k') i\mathcal{M}_C(p_2, p'_2; k, k'). \quad (2.8)$$

Here $\mathcal{M}_C(p_{\text{in}}, p_{\text{out}}; k_{\text{in}}, k_{\text{out}})$ denotes the amplitude of the tree-level Compton scattering $\psi(p_{\text{in}}) + a(k_{\text{in}}) \rightarrow \psi(p_{\text{out}}) + a(k_{\text{out}})$, which is calculated in App. C:

$$\mathcal{M}_C(p_{\text{in}}, p_{\text{out}}; k_{\text{in}}, k_{\text{out}}) = \frac{c_\psi^2}{f_a^2} m_\psi^2 \bar{u}(p_{\text{out}}) \left(\frac{\not{k}_{\text{in}}}{k_{\text{in}}^2 + 2k_{\text{in}} \cdot p_{\text{in}}} - \frac{\not{k}_{\text{out}}}{k_{\text{out}}^2 - 2k_{\text{out}} \cdot p_{\text{in}}} - \frac{1}{m_\psi} \right) u(p_{\text{in}}), \quad (2.9)$$

where $u(p)$ is the wavefunction of the external fermion with momentum p . As expected, we confirm in App. C that the calculations of the Compton scattering amplitude in both derivative basis and pseudoscalar basis provide the same result (2.9) up to $\mathcal{O}(1/f_a^2)$. Consequently, the amplitude in Eq. (2.8) agrees in both bases as well.

For the purpose of illustration, it is instructive to split \mathcal{M}_C into three parts:

$$\mathcal{M}_C \equiv \mathcal{M}_t^{\text{P}} + \mathcal{M}_u^{\text{P}} + \mathcal{M}_c^{\text{P}}, \quad (2.10)$$

according to the three terms in the bracket of Eq. (2.9). Here \mathcal{M}_t^p , \mathcal{M}_u^p , and \mathcal{M}_c^p correspond to the amplitude of the t -channel, u -channel, and contact scattering in the pseudoscalar basis, respectively, as shown in Fig. 13 and Eqs. (C.2)-(C.4). Then the multiplication of two \mathcal{M}_C in Eq. (2.8) can be schematically written as:

$$\begin{aligned} \mathcal{M}_C \mathcal{M}_C \sim & \underbrace{(\mathcal{M}_t^p \mathcal{M}_t^p + \mathcal{M}_u^p \mathcal{M}_u^p)}_{\text{Box 1}} + \underbrace{(\mathcal{M}_t^p \mathcal{M}_u^p + \mathcal{M}_u^p \mathcal{M}_t^p)}_{\text{Box 2}} + \underbrace{\mathcal{M}_c^p \mathcal{M}_c^p}_{\text{Bubble}} \\ & + \underbrace{(\mathcal{M}_t^p + \mathcal{M}_u^p) \mathcal{M}_c^p}_{\text{Triangle 1}} + \underbrace{\mathcal{M}_c^p (\mathcal{M}_t^p + \mathcal{M}_u^p)}_{\text{Triangle 2}}, \end{aligned} \quad (2.11)$$

where the text indicates the corresponding loop amplitude in Fig. 1 in the pseudoscalar basis. Therefore, the multiplication of the two \mathcal{M}_C in Eq. (2.8) indeed captures all the relevant loop diagrams in Fig. 1, with \mathcal{M}_C given by Eq. (2.9).

Next we turn to the axion propagators in Eq. (2.8). When both of the propagators take the vacuum part, it gives the amplitude of the two-axion force in vacuum [28, 30]. The effect from background corrections is extracted by taking the ‘‘crossing term’’, namely, only one of the propagators is on-shell:

$$\begin{aligned} i\mathcal{M}_{\text{bkg}} = & \int \frac{d^4 k}{(2\pi)^4} \int \frac{d^4 k'}{(2\pi)^4} (2\pi)^4 \delta^{(4)}(q+k-k') [D_{\text{bkg}}(k)D_{\text{vac}}(k') + D_{\text{vac}}(k)D_{\text{bkg}}(k')] \\ & \times i\mathcal{M}_C(p_1, p'_1; -k, -k') i\mathcal{M}_C(p_2, p'_2; k, k'). \end{aligned} \quad (2.12)$$

Substituting Eq. (2.6) into Eq. (2.12) one obtains:

$$\begin{aligned} \mathcal{M}_{\text{bkg}} = & - \int \frac{d^3 \mathbf{k}}{(2\pi)^3} f(\mathbf{k}) \int dk^0 \delta(k^2 - m_a^2) \Theta(k^0) \left[\frac{\mathcal{M}_C(p_1, p'_1; -k, -k-q) \mathcal{M}_C(p_2, p'_2; k, k+q)}{(k+q)^2 - m_a^2} \right. \\ & \left. + \frac{\mathcal{M}_C(p_1, p'_1; -k+q, -k) \mathcal{M}_C(p_2, p'_2; k-q, k)}{(k-q)^2 - m_a^2} \right], \end{aligned} \quad (2.13)$$

where we have performed the shift $k \rightarrow k - q$ in the second term in the bracket.

The existence of an axion background effectively violates the Lorentz symmetry through the time-independent phase-space distribution $f(\mathbf{k})$. Therefore, it is most convenient to first integrate out the time component k^0 using the δ -function, leading to

$$\begin{aligned} \mathcal{M}_{\text{bkg}} = & - \int \frac{d^3 k}{(2\pi)^3} \frac{f(\mathbf{k})}{2E_{\mathbf{k}}} \left[\frac{\mathcal{M}_C(p_1, p'_1; -k, -k-q) \mathcal{M}_C(p_2, p'_2; k, k+q)}{(k+q)^2 - m_a^2} \right. \\ & \left. + \frac{\mathcal{M}_C(p_1, p'_1; -k+q, -k) \mathcal{M}_C(p_2, p'_2; k-q, k)}{(k-q)^2 - m_a^2} \right] \Bigg|_{k^0=E_{\mathbf{k}}}, \end{aligned} \quad (2.14)$$

where $E_{\mathbf{k}} \equiv (\mathbf{k}^2 + m_a^2)^{1/2}$. According to Eq. (2.11), the contraction of two \mathcal{M}_C involves

multiple terms, which can be calculated separately. So we can write

$$\mathcal{M}_{\text{bkg}} = \mathcal{M}_{\text{box},1}^{\text{P}} + \mathcal{M}_{\text{box},2}^{\text{P}} + \mathcal{M}_{\text{tri},1}^{\text{P}} + \mathcal{M}_{\text{tri},2}^{\text{P}} + \mathcal{M}_{\text{bub}}^{\text{P}} , \quad (2.15)$$

where each term denotes the contribution from the corresponding diagram in Fig. 1 in the pseudoscalar basis. Taking the NR limit and expanding the wavefunctions up to the leading order of velocity and performing the Fourier transform in Eq. (2.5), we obtain the (spin-independent) background-induced axion force (see App. E for details):

$$V_{\text{bkg}}^{\text{inv}}(\mathbf{r}) = -\frac{c_1^2 c_2^2 m_1 m_2}{4\pi r f_a^4} \int \frac{d^3 \mathbf{k}}{(2\pi)^3} \frac{f(\mathbf{k})}{2E_{\mathbf{k}}} \mathcal{Q}_{\text{inv}} [\cos(|\mathbf{k}|r - \mathbf{k} \cdot \mathbf{r}) + \cos(|\mathbf{k}|r + \mathbf{k} \cdot \mathbf{r})] , \quad (2.16)$$

where $r \equiv |\mathbf{r}|$, $c_i \equiv c_{\psi_i}$ is the coupling in Eq. (2.2) between axion and ψ_i , and

$$\mathcal{Q}_{\text{inv}} = \sum_j \mathcal{Q}_j , \quad j = \text{box},1, \text{box},2, \text{tri},1, \text{tri},2, \text{bub} , \quad (2.17)$$

where

$$\mathcal{Q}_{\text{box},1} = \frac{2E_{\mathbf{k}}^2 m_1 m_2 (4E_{\mathbf{k}}^2 m_1 m_2 - m_a^4)}{(4m_1^2 E_{\mathbf{k}}^2 - m_a^4) (4m_2^2 E_{\mathbf{k}}^2 - m_a^4)} , \quad (2.18)$$

$$\mathcal{Q}_{\text{box},2} = \frac{2E_{\mathbf{k}}^2 m_1 m_2 (4E_{\mathbf{k}}^2 m_1 m_2 + m_a^4)}{(4m_1^2 E_{\mathbf{k}}^2 - m_a^4) (4m_2^2 E_{\mathbf{k}}^2 - m_a^4)} , \quad (2.19)$$

$$\mathcal{Q}_{\text{tri},1} = \frac{-4m_1^2 E_{\mathbf{k}}^2}{4m_1^2 E_{\mathbf{k}}^2 - m_a^4} , \quad (2.20)$$

$$\mathcal{Q}_{\text{tri},2} = \frac{-4m_2^2 E_{\mathbf{k}}^2}{4m_2^2 E_{\mathbf{k}}^2 - m_a^4} , \quad (2.21)$$

$$\mathcal{Q}_{\text{bub}} = 1 . \quad (2.22)$$

The result of the axion force in Eq. (2.16) and the \mathcal{Q} -factors in Eqs. (2.18)-(2.22) are valid up to leading order in the NR approximation, and are applicable for any axion background. Their derivations are provided in App. E. The values of \mathcal{Q} -factors in the hierarchical limit ($m_a \ll m_i$ or $m_a \gg m_i$) are collected in Tab. 1.

2.1.2 Order parameters

The \mathcal{Q} -factors play the role of the order parameters, which characterize the degree of shift-symmetry breaking. To see this, we add Eqs. (2.18)-(2.22) together and find that the terms that are not proportional to the power of the axion mass get exactly cancelled:

$$\mathcal{Q}_{\text{inv}} = \sum_j \mathcal{Q}_j = \frac{m_a^8}{(4m_1^2 E_{\mathbf{k}}^2 - m_a^4) (4m_2^2 E_{\mathbf{k}}^2 - m_a^4)} . \quad (2.23)$$

| Order Parameters | $\mathcal{Q}_{\text{box},1}$ | $\mathcal{Q}_{\text{box},2}$ | $\mathcal{Q}_{\text{tri},1}$ | $\mathcal{Q}_{\text{tri},2}$ | \mathcal{Q}_{bub} | \mathcal{Q}_{inv} |
|------------------|--|---|---|---|----------------------------|--|
| Full Expressions | (2.18) | (2.19) | (2.20) | (2.21) | (2.22) | (2.23) |
| $m_i \gg m_a$ | 1/2 | 1/2 | -1 | -1 | 1 | $\frac{m_a^8}{16m_1^2 m_2^2 E_{\mathbf{k}}^4}$ |
| $m_i \ll m_a$ | $-\frac{2E_{\mathbf{k}}^2 m_1 m_2}{m_a^4}$ | $\frac{2E_{\mathbf{k}}^2 m_1 m_2}{m_a^4}$ | $\frac{4m_1^2 E_{\mathbf{k}}^2}{m_a^4}$ | $\frac{4m_2^2 E_{\mathbf{k}}^2}{m_a^4}$ | 1 | 1 |

Table 1. The order parameters \mathcal{Q}_j (in the pseudoscalar basis) that break the shift symmetry of the diagram in Fig. 1. The background-induced axion force from each diagram is proportional to the corresponding order parameter. The order parameter with shift-invariant axion interaction (2.2) is given by the sum of five terms: $\mathcal{Q}_{\text{inv}} = \sum_j \mathcal{Q}_j$. The axion massless limit and heavy limit have been taken in the last two lines, respectively.

When there exists only shift-invariant interaction between axion and fermions [Eq. (2.2)], the axion mass is the only source that break the shift symmetry. As a result, the order parameter \mathcal{Q}_{inv} vanishes as $m_a \rightarrow 0$.

The background-induced force in Eq. (2.16) scales as $V_{\text{bkg}}^{\text{inv}} \sim \mathcal{Q}_{\text{inv}}/r$ at the leading order of the NR approximation, and thus vanishes as $m_a \rightarrow 0$. One may wonder why the $1/r$ long-range potential from the background correction disappears in the $m_a \rightarrow 0$ limit that corresponds to the restoration limit of the shift symmetry. This can be understood in the following way: First of all, as shown in App. D, the background effect only exists when there are at least two axions involved in the scattering process. The effective Hamiltonian responsible for the interaction between the fermion ψ and two axions can be written as

$$\mathcal{H}_{\text{eff}} = \frac{1}{\Lambda} \bar{\psi} \Gamma \psi a^2, \quad (2.24)$$

where Λ is the cutoff scale depending on the fermion mass and the axion decay constant, Γ denotes the possible Lorentz structure that is determined by calculating the elastic scattering $\psi + a \rightarrow \psi + a$ in Fig. 13. Note that Eq. (2.24) could result from the quadratic vertex in Fig. 13(c), as well from the combination of two linear vertices in Fig. 13(a) or 13(b). The $1/r$ potential is a typical tree-level effect, which (intuitively) is obtained by replacing one of the axion fields with its classical field value a_0 in Eq. (2.24):

$$\mathcal{H}_{\text{eff}} \rightarrow \mathcal{H}_{\text{eff,bkg}} = \frac{a_0}{\Lambda} \bar{\psi} \Gamma \psi a. \quad (2.25)$$

Then one can treat a_0/Λ as the constant coupling and the remaining part as an analogy of the Yukawa potential, getting $V_{\text{bkg}} \sim (a_0/\Lambda)^2/r$. However, in the absence of the shift-symmetry breaking, the classical field value a_0 can always be shifted to zero using the degree of freedom of shift invariance, which then forces V_{bkg} to vanish.

In general, the breaking of the shift symmetry is manifested in three effects that induce a nonvanishing long-range potential V_{bkg} : (a) the axion has a nonzero mass; (b) the

axion-fermion coupling explicitly breaks the shift symmetry; (c) the existence of the axion background sets a typical energy scale that effectively breaks the shift symmetry — this effect is more significant than the axion mass effect when background axions are relativistic. In scenario (a), V_{bkg} is suppressed by the power of the axion mass, making it difficult to detect. In Sec. 2.2, we will focus on scenarios (b) and (c).

2.1.3 Decoherence factor

There is a decoherence factor in Eq. (2.16):

$$\mathcal{D} \equiv \frac{1}{2} [\cos(|\mathbf{k}|r - \mathbf{k} \cdot \mathbf{r}) + \cos(|\mathbf{k}|r + \mathbf{k} \cdot \mathbf{r})]. \quad (2.26)$$

It describes the departure of V_{bkg} from a $1/r$ potential at long distances.

Suppose that the phase-space distribution $f(\mathbf{k})$ has a density around a peaked value $\mathbf{k} = \mathbf{k}_0$, then the typical de Broglie wavelength of the background axions is given by $\lambda_{\text{dB}} \sim 1/|\mathbf{k}_0|$. The background axions inside the volume λ_{dB}^3 can coherently scatter with the test particles. This can be seen from Eq. (2.26) by noticing that \mathcal{D} approaches 1 for $r \ll \lambda_{\text{dB}}$, and we have $V_{\text{bkg}} \sim 1/r$ in this case.

On the other hand, the background axion field at two places departing from $r \gtrsim \lambda_{\text{dB}}$ generically has different phases. As a result, their contributions to V_{bkg} are destructive, making it more suppressed than $1/r$. This is described by the cosine terms in Eq. (2.26), which have oscillating behaviors when the argument is larger than $\mathcal{O}(1)$ and kills the leading $1/r$ term after integrating over phase space. In most cases, due to the decoherence factor in Eq. (2.26), V_{bkg} is additionally suppressed by a factor of $(\lambda_{\text{dB}}/r)^n$ compared to $1/r$ at long distances $r \gg \lambda_{\text{dB}}$, where the power index n depends on the specific form of $f(\mathbf{k})$. We will show some concrete examples in Sec. 3.

Similar decoherence effects of background-induced forces at long distances have also been noticed recently in [32–34] for neutrinos and in [42, 43] for quadratically coupled scalar DM. We note that the form of the decoherence factor in Eq. (2.26) is slightly different from that in [42, 43]: Ref. [42] obtained $\mathcal{D} = \cos(|\mathbf{k}|r - \mathbf{k} \cdot \mathbf{r})$ while in Ref. [43] it is given by $\mathcal{D} = \cos(2\mathbf{k} \cdot \mathbf{r})$. Technically, the difference with respect to Ref. [42] arises since in Ref. [42] the decoherence factor was obtained by using retarded propagators for the off-shell mediator, while we used Feynman propagators (see App. E for more details). With regard to Ref. [43], they also used Feynman propagators, but the disagreement emerges from a different order of integration. While that does not affect the result in case of isotropic backgrounds, it does lead to a deviation for anisotropic backgrounds.¹ Note that the three expressions for \mathcal{D} reduce to 1 in the coherent region $r \ll \lambda_{\text{dB}}$; they also agree with each other after integrating over the phase space for isotropic backgrounds. There is, however, an $\mathcal{O}(1)$ difference between them for anisotropic backgrounds at $r \gtrsim \lambda_{\text{dB}}$.

¹We thank Sergio Barbosa and Sylvain Fichet for the correspondence about [43], in which they agreed on that point.

2.1.4 Further discussions

We close this subsection with a brief remark about other scenarios in which the formulae derived in this subsection can be used. Although Eqs. (2.16)-(2.22) are applicable for the axion force with only shift-invariant interactions, one can also use them to conveniently extract the background-induced force in theories with explicit shift-symmetry breaking:

- By replacing \mathcal{Q}_{inv} with \mathcal{Q}_{bub} in Eq. (2.16), one gets:

$$V_{\text{bkg}}^{\text{bub}}(\mathbf{r}) = -\frac{c_1^2 c_2^2 m_1 m_2}{4\pi r f_a^4} \int \frac{d^3 \mathbf{k}}{(2\pi)^3} \frac{f(\mathbf{k})}{E_{\mathbf{k}}} \mathcal{D}. \quad (2.27)$$

This is the background-induced force in a theory where the mediator is only quadratically coupled to the SM fermions: $\mathcal{L}_{\text{quad}} = c_i^2 m_i a^2 \bar{\psi}_i \psi_i / (2f_a^2)$, as studied in [42, 43].

- In addition, replace \mathcal{Q}_{inv} with the two box terms $\mathcal{Q}_{\text{box},1} + \mathcal{Q}_{\text{box},2}$ in Eq. (2.16):

$$V_{\text{bkg}}^{\text{box}}(\mathbf{r}) = -\frac{c_1^2 c_2^2 m_1 m_2}{4\pi r f_a^4} \int \frac{d^3 \mathbf{k}}{(2\pi)^3} \frac{f(\mathbf{k})}{E_{\mathbf{k}}} \frac{16E_{\mathbf{k}}^4 m_1^2 m_2^2}{(4m_1^2 E_{\mathbf{k}}^4 - m_a^4)(4m_2^2 E_{\mathbf{k}}^2 - m_a^4)} \mathcal{D}. \quad (2.28)$$

This corresponds to a theory where there is a pure pseudoscalar coupling: $\mathcal{L}_{\text{pseudo}} = -ic_i m_i a \bar{\psi}_i \gamma_5 \psi_i / f_a$. Note that in this case, the shift symmetry is explicitly broken by the fermion mass from the coupling. In the massless axion limit $m_a \ll m_i$, we have $\mathcal{Q}_{\text{box},1} + \mathcal{Q}_{\text{box},2} \approx 1$ and $V_{\text{bkg}}^{\text{box}}(r) \approx V_{\text{bkg}}^{\text{bub}}(r)$.

2.2 Breaking of the shift symmetry

We have seen from Sec. 2.1.2 that shift symmetry breaking is crucial to having a long-range $1/r$ axion force. In this subsection, we consider two scenarios of the axion shift symmetry breaking beyond the axion mass term and calculate their effects on V_{bkg} : (i) the non-perturbative effect induces a quadratic coupling between axions and fermions; (ii) the axion background modifies the dispersion relation of the axion propagator by enforcing it to be on-shell, which effectively violates the shift symmetry.

2.2.1 Quadratic coupling from non-perturbative effects

The axion quadratic terms explicitly break the shift symmetry. Note that although there is a quadratic coupling $a^2 \bar{\psi} \psi$ in Eq. (2.4), its contribution to the axion force is cancelled by the linear coupling, which coexists in the pseudoscalar basis. As a result, cancellation occurs among the order parameters in Eqs. (2.18)-(2.22), making the remaining term in Eq. (2.23) suppressed by the axion mass in the leading order of the NR approximation. This cancellation is expected because the shift symmetry is explicitly conserved in the derivative basis Eq. (2.3), which is equivalent to Eq. (2.4) up to $\mathcal{O}(1/f_a^2)$. In the following, we consider additional sources of quadratic coupling that are not related to the linear coupling.

We consider couplings that emerge from non-perturbative effects from the axion potential. They become relevant when the energy scale is below $\mu_0 \sim (m_a f_a)^{1/2}$ [see Eq. (1.1)], which

may induce a quadratic coupling between the axion and the SM fermions:

$$\mathcal{L}_\mu = \frac{\mu}{2f_a^2} a^2 \bar{\psi} \psi . \quad (2.29)$$

Here μ is a parameter with mass dimension one. For the QCD axion, the above effective coupling appears below the QCD confinement scale, and μ can be calculated using chiral perturbation theory (with ψ the nucleon): $\mu \equiv \mu_{\text{QCD}} \approx 15 \text{ MeV}$ [30, 35, 42]. In the more general cases of axion-like particles, μ is a free parameter that is determined by unknown ultraviolet (UV) physics. Since the coupling in Eq. (2.29) is induced below the non-perturbative scale, one may expect an upper bound of μ :

$$\mu \lesssim \sqrt{m_a f_a} . \quad (2.30)$$

The point to note is that μ can be much larger than the axion mass, which leads to a significant shift-symmetry-breaking effect compared to the mass term.

In [35], it was pointed out that the quadratic coupling (2.29) is important for the direct detection of axion DM through coherent scattering between axions and nucleons. Eq. (2.29) provides additional contributions to the diagrams in Fig. 1 and thus affects the axion force. The two-axion force in vacuum induced from Eq. (2.29) was calculated in [30]:

$$V_{2a}(r) = -\frac{\mu^2}{32\pi^3 f_a^4} \frac{m_a}{r^2} K_1(2m_a r) \quad (\text{vacuum two-axion force}) , \quad (2.31)$$

where K_1 is the modified Bessel function. The short- and long-range limits turn out to be:

$$\text{for } r \ll m_a^{-1} : \quad V_{2a}(r) = -\frac{\mu^2}{64\pi^3 f_a^4 r^3} , \quad (2.32)$$

$$\text{for } r \gg m_a^{-1} : \quad V_{2a}(r) = -\frac{\mu^2}{64\pi^3 f_a^4 r^3} \sqrt{\pi m_a r} e^{-2m_a r} . \quad (2.33)$$

At short distances, $V_{2a} \sim 1/r^3$ and is not suppressed by the axion mass. When the distance is larger than the inverse of the axion mass, V_{2a} starts to decrease exponentially — this is a typical feature of the quantum force where the propagators are off-shell.

Next we calculated the background-induced axion force caused by Eq. (2.29) and expressed it using the generic form of Eq. (2.1):

$$V_{\text{bkg}}^{\text{shft}}(\mathbf{r}; \mu) = -\frac{1}{4\pi r} \frac{m_1 m_2}{f_a^4} \int \frac{d^3 \mathbf{k}}{(2\pi)^3} \frac{f(\mathbf{k})}{E_{\mathbf{k}}} \left[\mathcal{Q}_{\text{tri}}^{\text{shft}}(\mu) + \mathcal{Q}_{\text{bub}}^{\text{shft}}(\mu) \right] \mathcal{D} , \quad (2.34)$$

where $\mathcal{Q}_{\text{tri}}^{\text{shft}}$ and $\mathcal{Q}_{\text{bub}}^{\text{shft}}$ are the order parameters induced by Eq. (2.29) that break the shift invariance. The first term denotes the contribution from two triangle diagrams, Fig. 1(c) and Fig. 1(d), which is a mixing effect between the quadratic coupling in Eq. (2.29) and the linear

coupling in Eq. (2.2):

$$\begin{aligned} \mathcal{Q}_{\text{tri}}^{\text{shft}}(\mu) &= -\frac{2\mu m_a^4 4E_{\mathbf{k}}^2 m_1 m_2 (c_1^2 m_2 + c_2^2 m_1) - m_a^4 (c_1^2 m_1 + c_2^2 m_2)}{m_1 m_2 (4E_{\mathbf{k}}^2 m_1^2 - m_a^4) (4E_{\mathbf{k}}^2 m_2^2 - m_a^4)} \\ &\approx -\frac{\mu m_a^4}{2m_1 m_2 E_{\mathbf{k}}^2} \left(\frac{c_1^2}{m_1} + \frac{c_2^2}{m_2} \right), \end{aligned} \quad (2.35)$$

where in the second line we used $m_a \ll m_i$. The second term comes from the bubble diagram, Fig. 1(e), that is purely induced by the quadratic coupling in Eq. (2.29):

$$\mathcal{Q}_{\text{bub}}^{\text{shft}}(\mu) = \frac{\mu^2}{m_1 m_2}. \quad (2.36)$$

Since $\mathcal{Q}_{\text{tri}}^{\text{shft}}$ is suppressed by the fourth power of the axion mass compared to $\mathcal{Q}_{\text{bub}}^{\text{shft}}$, it can be neglected for the practical detection of light axions. Then Eq. (2.34) is simplified to

$$V_{\text{bkg}}^{\text{shft}}(\mathbf{r}; \mu) = -\frac{\mu^2}{4\pi r f_a^4} \int \frac{d^3 \mathbf{k}}{(2\pi)^3} \frac{f(\mathbf{k})}{2E_{\mathbf{k}}} [\cos(|\mathbf{k}|r - \mathbf{k} \cdot \mathbf{r}) + \cos(|\mathbf{k}|r + \mathbf{k} \cdot \mathbf{r})]. \quad (2.37)$$

Therefore, at the leading order, the magnitude of V_{bkg} is controlled by the non-perturbative scale μ .

In the following, we discuss two special cases of interest.

(i) For the isotropic axion background $f(\mathbf{k}) = f(\kappa)$ with $\kappa \equiv |\mathbf{k}|$, one can first integrate out the angular part of the phase space, leading to

$$V_{\text{bkg}}^{\text{iso}}(r; \mu) = -\frac{\mu^2}{16\pi^3 r^2 f_a^4} \int_0^\infty d\kappa \frac{\kappa f(\kappa)}{\sqrt{\kappa^2 + m_a^2}} \sin(2\kappa r). \quad (2.38)$$

This agrees with the result in [42, 43] with effective quadratic couplings of scalars for isotropic backgrounds.

(ii) In the coherent region $r \ll \lambda_{\text{dB}}$, we have $\mathcal{D} \rightarrow 1$, and Eq. (2.37) is reduced to

$$V_{\text{bkg}}^{\text{coh}}(r; \mu) = -\frac{\mu^2}{4\pi r f_a^4} \int \frac{d^3 \mathbf{k}}{(2\pi)^3} \frac{f(\mathbf{k})}{E_{\mathbf{k}}} = -\frac{\mu^2 \tilde{n}_a}{4\pi r f_a^4 m_a}, \quad (2.39)$$

where \tilde{n}_a is the effective number density of background axions, defined as:

$$\tilde{n}_a \equiv \int \frac{d^3 \mathbf{k}}{(2\pi)^3} \frac{f(\mathbf{k})}{E_{\mathbf{k}}/m_a}. \quad (2.40)$$

In particular, for NR axion backgrounds $E_{\mathbf{k}} \approx m_a$, then \tilde{n}_a is reduced to the usual number

density n_a , and we have

$$V_{\text{bkg,NR}}^{\text{coh}}(r; \mu) = -\frac{\mu^2 \rho_a}{4\pi r f_a^4 m_a^2}, \quad (2.41)$$

where $\rho_a = m_a n_a$ is the energy density of the NR axion background. In this region, V_{bkg} is insensitive to the specific distribution function $f(\mathbf{k})$ and is enhanced by $1/m_a^2$ for a fixed ρ_a . The result of Eq. (2.41) agrees with that derived in [20, 37] using classical field theories.

From the theoretical point of view, one cannot keep increasing the magnitude of $V_{\text{bkg,NR}}^{\text{coh}}$ by infinitely decreasing m_a in Eq. (2.41). To see this, we recall that the NR energy density ρ_a can be connected to the axion classical field value a_0 via $\rho_a \sim m_a^2 a_0^2$. However, the validity of the axion effective interaction requires $a_0 \lesssim f_a$ (otherwise, the axion potential is anharmonic, and one needs to include the nonlinear corrections from axion self-interactions). As a result, we have $\rho_a \lesssim m_a^2 f_a^2$ and Eq. (2.41) is bounded from

$$\left| V_{\text{bkg,NR}}^{\text{coh}}(r; \mu) \right| \lesssim \frac{\mu^2}{4\pi r f_a^2}. \quad (2.42)$$

Note that under the assumption of $a_0 \lesssim f_a$, the contribution to V_{bkg} from n -axion exchange (with $n > 2$) is more suppressed compared to that from two-axion exchange, and hence can be neglected.

A comparison between V_{bkg} and V_{2a} is shown in Fig. 3, see Sec. 4 for more discussions.

2.2.2 Effective shift-symmetry breaking from axion backgrounds

Suppose there is an axion background with the phase-space distribution function $f(\mathbf{k}; \mathbf{k}_0)$, in which we assume the momentum distribution is peaked around $\mathbf{k} = \mathbf{k}_0$. It sets a typical energy scale $(\mathbf{k}_0^2 + m_a^2)^{1/2}$. If the background axions are relativistic, i.e., $|\mathbf{k}_0| \gg m_a$, then $|\mathbf{k}_0|$ plays the role of the order parameter to effectively break the shift symmetry.

This can be seen by including the relativistic correction to Eq. (2.16). Note that to get Eq. (2.16) we have taken the NR limit, which means that we neglected all terms suppressed by higher orders of \mathbf{q}^2 . Terms with higher orders of \mathbf{q}^2 result in derivative operators after the Fourier transform. In vacuum, the derivative operators increase the power index n of a $1/r^n$ potential, making it more suppressed at long distances. However, when there is a background, the derivative can act on the decoherence factor $\cos(|\mathbf{k}|r \pm \mathbf{k} \cdot \mathbf{r})$ that is not a polynomial function of r ; in this case, the final effect is to replace \mathbf{q}^2 with \mathbf{k}_0^2 . Therefore, terms with higher orders of \mathbf{q}^2 can still lead to a $1/r$ potential in the axion background, which is proportional to the power of the typical energy scale of the background.

The relativistic correction of V_{bkg} is calculated in App. E.1, with the final expression given by Eq. (E.29). Note that we have taken $m_a = 0$ because we assume that the axion background is relativistic and we are interested in the effect of shift symmetry breaking that comes purely from the background. The result in Eq. (E.29) contains multiple terms of $1/r^5$, $1/r^4$, $1/r^3$, $1/r^2$, and $1/r$. For $r \gg 1/|\mathbf{k}_0|$, which is satisfied for most fifth-force experiments

with a relativistic axion background, the $1/r$ term becomes dominant, then we obtain:

$$V_{\text{bkg}}^{\text{rel}}(\mathbf{r}) = -\frac{c_1^2 c_2^2}{64\pi m_1 m_2 f_a^4} \times \frac{1}{r} \times \int \frac{d^3\mathbf{k}}{(2\pi)^3} \frac{|\mathbf{k}|^4}{E_{\mathbf{k}}} f(\mathbf{k}; \mathbf{k}_0) (1 - 3c^2 + 3c^4) \mathcal{D}, \quad (2.43)$$

where the index “rel” implies the relativistic correction from the axion background, \mathcal{D} is given by Eq. (2.26) and $c \equiv \cos(\hat{\mathbf{k}} \cdot \hat{\mathbf{r}})$ denotes the cosine of the angle between \mathbf{k} and \mathbf{r} . After the phase-space integral, the momentum \mathbf{k} in Eq. (2.43) is typically replaced by its central value \mathbf{k}_0 . Comparing with the parametric form in Eq. (2.1), we find the order parameter in a relativistic axion background is given by

$$\mathcal{Q}_{\text{rel}}(\mathbf{k}_0) = \frac{|\mathbf{k}_0|^4}{16m_1^2 m_2^2}. \quad (2.44)$$

Note that the NR approximation of the external fermions ψ_i holds when $|\mathbf{k}_0| \ll m_i$, which causes a suppression to \mathcal{Q}_{rel} . Nevertheless, the order parameter in Eq. (2.44) can still be much larger than that in Eq. (2.23) given an energetic axion background satisfying $|\mathbf{k}_0| \gg m_a$. A typical example is the solar axion flux with $|\mathbf{k}_0| \sim \text{keV}$, as will be discussed in Sec. 4.2.

2.3 Summary

We have derived the general formulae for the background-induced axion force V_{bkg} , with a generic form described by Eq. (2.1). In the absence of shift-symmetry-breaking interactions, cancellations occur among different diagrams, causing a suppression to the final result. In the NR limit, V_{bkg} is given by Eq. (2.16), where the axion mass plays the role of order parameter that breaks the shift symmetry. There are two possibilities to enhance V_{bkg} . First, the non-perturbative effect from the axion potential induces a quadratic coupling that explicitly breaks the shift symmetry, leading to a much larger V_{bkg} in Eq. (2.37). Second, the axion background effectively breaks the shift symmetry; this effect appears as relativistic corrections of the NR scattering amplitude. In an energetic axion background with a typical momentum $|\mathbf{k}_0| \gg m_a$, V_{bkg} is enhanced by a factor of $|\mathbf{k}_0|^4/m_a^4$, as shown in Eq. (2.43).

3 Typical axion backgrounds

In this section, we apply the general formulae derived in Sec. 2 to several well-motivated axion backgrounds: Maxwell-Boltzmann (MB) distribution, Bose-Einstein (BE) distribution, and relativistic axion flux. They correspond to the ideal situations of three typical axion sources, respectively: cold axion DM, thermal axion relics, and solar axion flux. For each example, we calculate the specific V_{bkg} using Eqs. (2.16), (2.37) and (2.43). We leave the discussion of experimental probes to Sec. 4.

3.1 Maxwell-Boltzmann distribution

As a first example, we consider the following isotropic MB distribution:

$$f_{\text{MB}}(\kappa) = n_a (2\pi)^{3/2} \kappa_0^{-3} e^{-\kappa^2/(2\kappa_0^2)}, \quad (3.1)$$

where $n_a = \int d^3\mathbf{k} f_{\text{MB}}(\kappa)/(2\pi)^3$ is the number density and κ_0 characterizes the momentum dispersion. Eq. (3.1) coincides with the NR limit of the thermal MB distribution with an effective temperature T_a : $e^{-E\mathbf{k}/T_a} \rightarrow e^{-\kappa^2/(2m_a T_a)}$. Note that the dynamics of cold DM in the galaxy is dominated by gravitational interactions, and the DM particles are not in thermal equilibrium. However, N -body simulation indicates that the DM phase-space distribution in the galaxy can still be approximately described by the Gaussian form in Eq. (3.1) [59–62]. (The more realistic DM distribution has anisotropy due to the motion of the Earth, which will be discussed in Sec. 4.1). The momentum dispersion is estimated by $\kappa_0 \approx m_a v_a/\sqrt{2}$ with $v_a \sim \mathcal{O}(10^{-3})$ the local velocity of the DM halo.

We first calculate V_{bkg} with the shift-invariant interaction. For NR axion background, assuming $m_a \ll m_i$, the order parameter (2.23) is reduced to $Q_{\text{inv}} \approx m_a^4/(16m_1^2 m_2^2)$. Substituting it into Eq. (2.16) and performing the integral one obtains

$$\begin{aligned} V_{\text{MB}}^{\text{inv}}(r) &= -\frac{c_1^2 c_2^2 m_a^3}{256\pi^3 r^2 f_a^4 m_1 m_2} \int_0^\infty d\kappa \kappa f_{\text{MB}}(\kappa) \sin(2\kappa r) \\ &= -\frac{c_1^2 c_2^2 \rho_a m_a^2}{64\pi r f_a^4 m_1 m_2} e^{-2\kappa_0^2 r^2}, \end{aligned} \quad (3.2)$$

where in the second line we have used the relation $\rho_a = m_a n_a$ for NR axions. Note that the potential in Eq. (3.2) is suppressed by $m_a^2/(m_1 m_2)$ for light axions. Due to the decoherence factor in Eq. (2.26), the isotropic MB distribution leads to an exponential suppression to V_{bkg} at large distances $r \gg \lambda_{\text{dB}} \sim 1/\kappa_0$; while for $r \ll 1/\kappa_0$, V_{bkg} exhibits the generic $1/r$ behavior. Similar results were also derived in [42, 43] with effective quadratic couplings.

We proceed to calculate V_{bkg} with explicit shift-symmetry breaking using Eq. (2.38). It turns out to be

$$V_{\text{MB}}^{\text{shift}}(r; \mu) = -\frac{\mu^2 \rho_a}{4\pi r f_a^4 m_a^2} e^{-2\kappa_0^2 r^2}. \quad (3.3)$$

Note that Eq. (3.3) can also be obtained from Eq. (3.2) by simply replacing the order parameter $Q_{\text{inv}} = m_a^4/(16m_1^2 m_2^2)$ with that in Eq. (2.36).

Since the axion background considered in this case is NR, the relativistic correction from Eq. (2.43) is more suppressed than that in Eq. (3.2) and hence can be neglected.

3.2 Bose-Einstein distribution

If axions were thermally produced in the early universe and then relativistically decoupled from the SM bath at some temperature T_d , they remain as the thermal relics to the present

day that obey the BE distribution [56]:

$$f_{\text{BE}}(\kappa) = \frac{1}{e^{\kappa/T_a} - 1}, \quad (3.4)$$

where T_a is the axion effective temperature at the present day, given by

$$T_a = \left[\frac{g_{*S}(T_0)}{g_{*S}(T_d)} \right]^{\frac{1}{3}} T_0 \equiv \xi_a T_0, \quad (3.5)$$

where $T_0 \approx 2.7 \text{ K} \approx 0.23 \text{ meV}$ is the temperature of today's cosmic microwave background (CMB), $g_{*S}(T)$ is the relativistic degree of freedom relevant to the entropy at temperature T . The discrepancy between T_a and T_d appears because the SM thermal bath can be reheated after axion decoupling (with entropy conserved), as characterized by the factor $\xi_a \leq 1$. The precise value of ξ_a depends on T_d , which is determined by the couplings between axions and SM particles. If axions were relativistic when decoupling, their contribution to the effective neutrino number N_{eff} at the CMB epoch can be written as

$$\Delta N_{\text{eff}} = \frac{4}{7} \left(\frac{11}{4} \right)^{\frac{4}{3}} \left(\frac{T_a}{T_0} \right)^4. \quad (3.6)$$

The recent CMB constraint $\Delta N_{\text{eff}} \lesssim 0.285$ [63] requires $\xi_a \lesssim 0.6$ or $T_a \lesssim 0.14 \text{ meV}$. As an estimate, we take $T_a = 10^{-4} \text{ eV}$ in the following discussion.

The relativistic correction (2.43) is only relevant for $m_a \ll T_a$. However, even in this case, it is still highly suppressed by $T_a^4/(m_1^2 m_2^2)$ and thus can be neglected. On the other hand, using the BE distribution, Eqs. (2.16) and (2.37) are reduced to

$$V_{\text{BE}}^{\text{inv}}(r) = -\frac{c_1^2 c_2^2 m_a^8}{256 \pi^3 r^2 f_a^4 m_1 m_2} \int_0^\infty d\kappa \frac{\kappa \sin(2\kappa r)}{(\kappa^2 + m_a^2)^{5/2} (e^{\kappa/T_a} - 1)}, \quad (3.7)$$

$$V_{\text{BE}}^{\text{shft}}(r; \mu) = -\frac{\mu^2}{16 \pi^3 r^2 f_a^4} \int_0^\infty d\kappa \frac{\kappa \sin(2\kappa r)}{(\kappa^2 + m_a^2)^{1/2} (e^{\kappa/T_a} - 1)}. \quad (3.8)$$

We discuss two hierarchical limits:

(i) Relativistic relic axions with $m_a \ll 10^{-4} \text{ eV}$. In this case, $V_{\text{BE}}^{\text{inv}}$ is negligible because of the suppression of the axion mass, while $V_{\text{BE}}^{\text{shft}}$ is given by

$$\begin{aligned} V_{\text{BE}}^{\text{shft}}(r; \mu) &= -\frac{\mu^2}{64 \pi^3 r^3 f_a^4} [2\pi r T_a \coth(2\pi r T_a) - 1] \\ &= -\frac{\mu^2}{64 \pi^3 f_a^4} \begin{cases} 4\pi^2 T_a^2 / (3r) & \text{for } r \ll T_a^{-1} \\ 2\pi T_a / r^2 & \text{for } r \gg T_a^{-1} \end{cases}. \end{aligned} \quad (3.9)$$

The typical de Broglie wavelength of axion relics is characterized by the axion temperature $\lambda_{\text{dB}} \sim 1/T_a$, while the number density scales as $n_a \sim T_a^3$. Comparing Eq. (3.9) with (2.1), we

find that the decoherence factor causes an additional suppression $1/(T_a r)$ compared to a $1/r$ potential at long distances $r \gg \lambda_{\text{dB}}$.

(ii) NR relic axions with $m_a \gg 10^{-4}$ eV. In this case, we arrive at

$$\begin{aligned} V_{\text{BE}}^{\text{shft}}(r; \mu) &= \frac{16\mu^2 m_1 m_2}{m_a^4} V_{\text{BE}}^{\text{inv}}(r) \\ &= -\frac{\mu^2 T_a^2}{32\pi^3 f_a^4 m_a r^2} \left[i\psi^{(1)}(1 + 2irT_a) - i\psi^{(1)}(1 - 2irT_a) \right] \\ &= -\frac{\mu^2}{32\pi^3 f_a^4 m_a} \begin{cases} 8\zeta(3)T_a^3/r & \text{for } r \ll T_a^{-1} \\ T_a/r^3 & \text{for } r \gg T_a^{-1} \end{cases}, \end{aligned} \quad (3.10)$$

where $\zeta(3) \approx 1.202$, $\psi^{(n)}$ is the n -th ordered polygamma function, defined as

$$\psi^{(n)}(x) \equiv \frac{d^{n+1}}{dx^{n+1}} \log \Gamma(x)$$

with $\Gamma(x)$ being the gamma function. From Eq. (3.10), it can be seen that for NR relic axions, the suppression caused by the decoherence effect is $1/(T_a r)^2$ when $r \gg \lambda_{\text{dB}}$.

If the relic axions are NR today, their energy density is given by

$$\rho_a = m_a n_a = m_a \int \frac{d^3\mathbf{k}}{(2\pi)^3} \frac{1}{e^{\kappa/T_a} - 1} = \frac{\zeta(3)}{\pi^2} m_a T_a^3. \quad (3.11)$$

By asking ρ_a to not exceed the total relic abundance of DM, one obtains a conservative upper bound on the axion mass if axions comprise the thermal relics at present:

$$m_a \lesssim 80 \text{ eV}, \quad (3.12)$$

which may be relaxed if T_a is below 10^{-4} eV.

3.3 Relativistic axion flux

We consider an energetic axion flux with good direction and typical momentum $\kappa_0 \gg m_a$. The phase-space distribution function can be written as

$$f_{\text{flux}}(\mathbf{k}) = (2\pi)^3 \frac{d\Phi}{d\kappa} \delta(\hat{\mathbf{k}} - \hat{\mathbf{k}}_0), \quad (3.13)$$

where the unit vector $\hat{\mathbf{k}}_0$ denotes the direction of the flux, $d\Phi/d\kappa$ is the differential flux (i.e., the flux per energy) with the peaked value at $\kappa = \kappa_0$ and normalized as

$$\int \frac{d^3\mathbf{k}}{(2\pi)^3} f_{\text{flux}}(\mathbf{k}) = \Phi, \quad (3.14)$$

with Φ the total flux.

Since the flux is relativistic, one can neglect the contribution from Eq. (2.16) that is suppressed by the axion mass. Substituting Eq. (3.13) into Eqs. (2.37) and (2.43), we obtain

$$V_{\text{flux}}^{\text{shft}}(r, \alpha; \mu) = -\frac{\mu^2}{4\pi r f_a^4} \int_0^\infty \frac{d\kappa}{\kappa} \frac{d\Phi}{d\kappa} \cos(\kappa r) \cos(\kappa r \cos \alpha), \quad (3.15)$$

$$V_{\text{flux}}^{\text{rel}}(r, \alpha) = -\frac{c_1^2 c_2^2}{64\pi r m_1 m_2 f_a^4} \int_0^\infty d\kappa \kappa^3 \frac{d\Phi}{d\kappa} (1 - 3\cos^2 \alpha + 3\cos^4 \alpha) \cos(\kappa r) \cos(\kappa r \cos \alpha), \quad (3.16)$$

where α is the angle between $\hat{\mathbf{k}}_0$ and \mathbf{r} . Note that the momentum spread and the finite size of the object will lead to oscillations when the argument of the cosine function is much larger than 1, which makes the potential more suppressed than $1/r$. The condition to avoid the decoherence suppression is given by

$$\alpha^2 \lesssim \pi/\Delta(\kappa r), \quad (3.17)$$

where $\Delta(\kappa r)$ denotes the spread of κr . For example, for $\Delta(\kappa r) = \text{keV} \cdot \text{cm}$, this condition implies $\alpha \lesssim 10^{-4}$. In the ideal case of the small-angle limit, Eqs. (3.15)-(3.16) are reduced to

$$V_{\text{flux}}^{\text{shft}}(r; \mu) = -\frac{\mu^2}{8\pi r f_a^4} \int_0^\infty \frac{d\kappa}{\kappa} \frac{d\Phi}{d\kappa}, \quad (3.18)$$

$$V_{\text{flux}}^{\text{rel}}(r) = -\frac{c_1^2 c_2^2}{128\pi r m_1 m_2 f_a^4} \int_0^\infty d\kappa \kappa^3 \frac{d\Phi}{d\kappa}. \quad (3.19)$$

The relativistic axion beam with a fixed direction corresponds to a realistic scenario — the axion flux emitted from the Sun, which will be discussed in Sec. 4.2.

4 Experimental probes of the axion forces

Here we move to discuss ways to probe the axion force. One way to probe the force is through fifth-force detection experiments. The long-range axion force between two objects contributes as a correction to gravity, which may leave imprints in the precision tests of gravitational inverse-square law and equivalence principle (see e.g. [74–76] for a review).

Assuming the existence of axions and axion backgrounds, the (spin-independent) long-range potential between two objects can be written as

$$V(r) = V_{\text{grav}}(r) + V_{2a}(r) + V_{\text{bkg}}(r) \equiv V_{\text{grav}}(r) + \delta V(r), \quad (4.1)$$

where V_{grav} denotes the Newtonian potential, V_{2a} is the vacuum two-axion potential given in Eq. (2.31), and V_{bkg} is the background-induced axion force. In Table 2, we collect the sensitivities and length scales of typical experiments that aim to detect the fifth force.

The vacuum axion force V_{2a} suffers from exponential suppression at long distances $r \gg 1/m_a$. On the other hand, V_{bkg} remains $1/r$ as long as $r \ll \lambda_{\text{dB}}$. Note that for cold DM

| Experiments | $\delta V / V_{\text{grav}}$ | $\langle r \rangle$ | Refs |
|--------------------------------|------------------------------|----------------------|------|
| MICROSCOPE | 3.8×10^{-15} | $\sim 7100\text{km}$ | [64] |
| Washington2007 | 1.8×10^{-13} | $\sim 6400\text{km}$ | [65] |
| Washington1999 | 3.0×10^{-9} | $\sim 0.3\text{m}$ | [66] |
| Irvine1985 | 7×10^{-5} | $2 - 5\text{cm}$ | [67] |
| HUST2012 | 10^{-3} | $\sim 2\text{mm}$ | [68] |
| Eöt-Wash2006 | 2×10^{-3} | $\sim 0.5\text{mm}$ | [69] |
| HUST2020 | 3×10^{-3} | $\sim 0.3\text{mm}$ | [70] |
| Washington2020 | ~ 1 | $52\mu\text{m}$ | [71] |
| Future levitated optomechanics | $\sim 10^4$ | $1\mu\text{m}$ | [72] |
| IUPUI2014 | 2.7×10^7 | 560nm | [73] |

Table 2. The sensitivities of typical fifth-force search experiments. Here V_{grav} is the Newtonian potential, while δV is the contribution from long-range forces other than gravity. The third column lists the typical length scale of the corresponding experiment.

with local velocity $v_a \sim 10^{-3}$, we have $\lambda_{\text{dB}} \sim 1/(m_a v_a) \sim 10^3/m_a$, which is three orders of magnitude larger than the range of V_{2a} . In Fig. 3, we compare the magnitude of V_{bkg} with V_{2a} in the coherent region assuming a cold DM background. As one can see, for small axion masses, V_{bkg} is enhanced by $1/m_a^2$, while for large axion masses $m_a \gg 1/r$, V_{2a} is exponentially suppressed. As a result, V_{bkg} dominates over V_{2a} at the length scales of most fifth-force search experiments. At $r \gtrsim \lambda_{\text{dB}}$, V_{bkg} is additionally suppressed due to the decoherence effect, but in most cases (except for the isotropic MB discussed in Sec. 3.1) the suppression is less than the exponential suppression. Based on the above argument, we will neglect the contribution from V_{2a} and assume $\delta V = V_{\text{bkg}}$.

In the following two subsections, we calculate the effect of V_{bkg} on the fifth-force detection by assuming two independent axion backgrounds: (1) axion cold DM and (2) solar axion flux. A different detection method using atomic spectroscopy is discussed in Sec. 4.3.

4.1 Axion dark matter

Since the axion DM background is non-relativistic, the relevant V_{bkg} comes from Eq. (2.37), induced by the quadratic coupling and dominant for light axions, and from Eq. (2.16), induced by the axion mass and only relevant for heavy axions. We will refer to them as “ μ -term” and “mass term” in the following discussion, respectively.

4.1.1 Coherent limit

Before diving into the specific phase-space distribution, let us first make the most optimistic estimate, i.e., take the coherent limit $r \ll \lambda_{\text{dB}}$. In this case, V_{bkg} induced from μ -term is given by Eq. (2.41), a typical $1/r$ long-range potential. We further assume that the size of the object is smaller than λ_{dB} , such that all particles in the object can contribute coherently

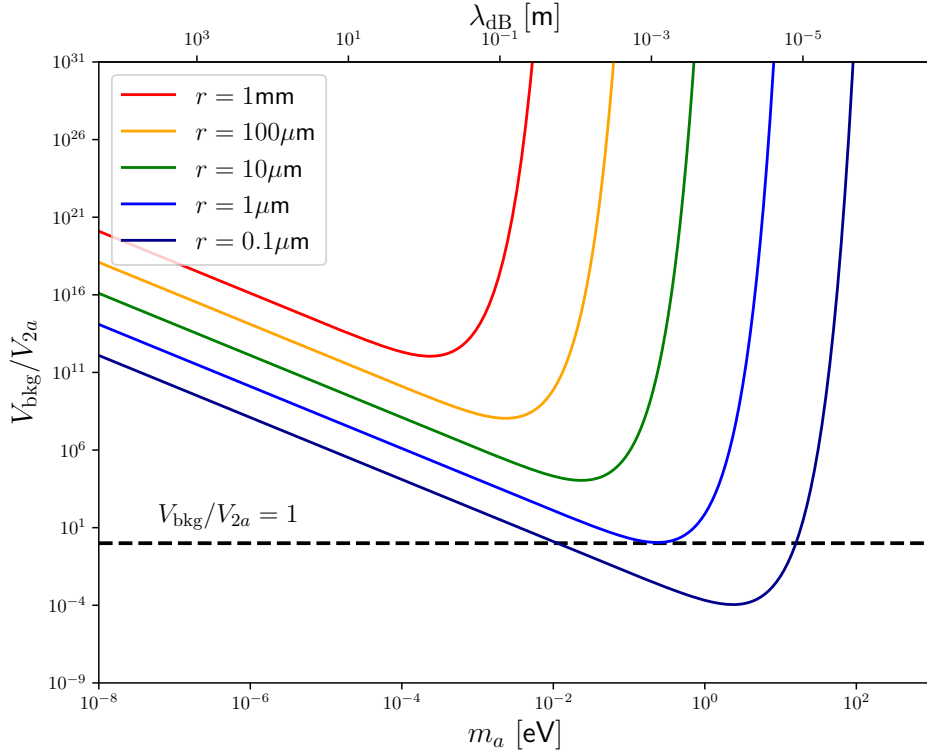


Figure 3. The comparison between the background-induced axion force V_{bkg} in the coherent region [Eq. (2.41)] and its vacuum counterpart V_{2a} [Eq. (2.31)]. Note that the dependence on both μ and f_a is cancelled in the ratio V_{bkg}/V_{2a} , indicating that these two terms are of the same order from the view of effective field theories. We have fixed $\rho_a = \rho_{\text{DM}} \approx 0.4 \text{ GeV/cm}^3$ as the local density of DM. We also take the typical de Broglie wavelength as $\lambda_{\text{dB}} = 1/(m_a v_a)$, with $v_a \approx 10^{-3}$ the average velocity of the axion DM. Different curves in the plot correspond to the comparison at different length scales.

to V_{bkg} . Comparing the axion force with the gravity, we obtain

$$\frac{\delta V_{\mu\text{-term}}}{V_{\text{grav}}} = \frac{\mu^2 \rho_a N_1 N_2}{4\pi r f_a^4 m_a^2} \bigg/ \frac{G_N M_1 M_2}{r} = \frac{2\mu^2 \rho_a M_{\text{Pl}}^2}{f_a^4 m_a^2 m_N^2}, \quad (4.2)$$

where M_i and N_i are the mass and number of particles of object $i = 1, 2$, $M_1/N_1 \approx M_2/N_2 \approx m_N \approx 1 \text{ GeV}$ is the average nucleon mass, and $M_{\text{Pl}} = 1/\sqrt{8\pi G_N} \approx 2.4 \times 10^{18} \text{ GeV}$ is the reduced Planck mass with G_N the gravitational constant. We assume that axions constitute the entire cold DM and take $\rho_a = \rho_{\text{DM}} \approx 0.4 \text{ GeV/cm}^3$, the DM energy density in the local galaxy. For QCD axion, we have $\mu = \mu_{\text{QCD}} \approx 15 \text{ MeV}$ and $m_a f_a \approx 5.7 \times 10^{-3} \text{ GeV}^2$ [77], leading to

$$\left(\frac{\delta V_{\mu\text{-term}}}{V_{\text{grav}}} \right)_{\text{QCD axion}} \approx 10^{-15} \left(\frac{5 \times 10^5 \text{ GeV}}{f_a} \right)^2, \quad (4.3)$$

where $\delta V/V_{\text{grav}} \sim 10^{-15}$ is the sensitivity of MICROSCOPE experiment [64]. For generic axion-like particles, μ is determined by UV models responsible for the shift symmetry breaking. Here we take the upper bound of $\mu \lesssim \sqrt{m_a f_a}$ [see Eq. (2.30)] as an estimate:

$$\left(\frac{\delta V_{\mu\text{-term}}}{V_{\text{grav}}}\right)_{\text{ALP}} \approx 10^{-15} \left(\frac{10^{-21} \text{ eV}}{m_a}\right) \left(\frac{3 \times 10^{13} \text{ GeV}}{f_a}\right)^3. \quad (4.4)$$

Although axions are usually considered to be light particles (sub-eV), there are still possibilities that axions can have a much heavier mass, see [78–87] for the theoretical efforts. In this case, the V_{bkg} induced by the mass term is not negligible. Yet, we still assume that the axion is lighter than the nucleon, $m_a \lesssim m_N$. Taking the coherent limit in Eq. (2.16) to maximize the effect, we obtain

$$\frac{\delta V_{\text{mass-term}}}{V_{\text{grav}}} = \frac{c_N^4 m_a^2 \rho_a M_{\text{Pl}}^2}{8 f_a^4 m_N^4} \approx 10^{-15} \left(\frac{m_a}{\text{GeV}}\right)^2 \left(\frac{2 \times 10^2 \text{ GeV}}{f_a/c_N}\right)^4, \quad (4.5)$$

where c_N is the dimensionless axion coupling in Eq. (2.3) with ψ to be the nucleon.

4.1.2 Decoherence effect

The realistic distribution of axion DM may lead to additional suppression compared to a $1/r$ potential due to the decoherence factor in Eq. (2.26). As mentioned in Sec. 3.1, the actual distribution of DM in the local galaxy is not isotropic; it has a preferred direction because of the Earth’s motion relative to the DM halo. This can be described by the boosted Maxwell-Boltzmann (BMB) distribution:

$$\begin{aligned} f_{\text{BMB}}(\mathbf{k}) &= f_{\text{MB}}(\mathbf{k} - m_a \mathbf{v}_a) \\ &= n_a (2\pi)^{3/2} \kappa_0^{-3} \exp\left(-\frac{|\mathbf{k} - m_a \mathbf{v}_a|^2}{2\kappa_0^2}\right), \end{aligned} \quad (4.6)$$

where f_{MB} is given in Eq. (3.1), \mathbf{v}_a is the velocity of the Earth relative to the galaxy center with $v_a \equiv |\mathbf{v}_a| \approx 220 \text{ km/s}$, and $\kappa_0 = m_a v_a / \sqrt{2}$ is the momentum dispersion according to the Standard Halo Model [88].

Point-like object

We first assume that the size of the test objects is negligible. Combining Eq. (4.6) with Eqs. (2.16) and (2.37), the relevant background-induced axion forces between two point-like objects are given by

$$\mu\text{-term: } V_{\text{bkg,point}}^{\text{shift}}(\mathbf{r}; \mu) = -\frac{\mu^2 \rho_a}{4\pi f_a^4 m_a^2} \frac{\mathcal{F}_{\text{PS}}(\mathbf{r})}{r}, \quad (4.7)$$

$$\text{mass-term: } V_{\text{bkg,point}}^{\text{inv}}(\mathbf{r}) = -\frac{c_N^4 \rho_a m_a^2}{64\pi f_a^4 m_N^2} \frac{\mathcal{F}_{\text{PS}}(\mathbf{r})}{r}, \quad (4.8)$$

where the dimensionless phase-space form factor is defined as

$$\mathcal{F}_{\text{PS}}(\mathbf{r}) \equiv \int \frac{d^3\mathbf{k}}{(2\pi)^3} \frac{f_{\text{BMB}}(\mathbf{k})}{n_a} \mathcal{D}, \quad (4.9)$$

with \mathcal{D} given by Eq. (2.26). \mathcal{F}_{PS} characterizes the decoherence effect from the phase-space spread. Note that the form factor defined in Eq. (4.9) matches that in [42] by replacing \mathcal{D} with $\cos(|\mathbf{k}|r - \mathbf{k} \cdot \mathbf{r})$.

By explicit calculation, we obtain (see App. F for details)

$$\begin{aligned} \mathcal{F}_{\text{PS}}(r, \alpha) &= \frac{e^{-1}}{\sqrt{2\pi} \kappa_0^3} \int_0^\infty d\kappa \kappa^2 \cos(\kappa r) e^{-\frac{\kappa^2}{2\kappa_0^2}} \\ &\quad \times \int_{-1}^1 dz e^{\frac{\sqrt{2}\kappa z}{\kappa_0}} \cos(\kappa r \cos \alpha z) J_0\left(\kappa r \sin \alpha \sqrt{1-z^2}\right), \end{aligned} \quad (4.10)$$

where α is the angle between \mathbf{r} and \mathbf{v}_a , and J_0 is the Bessel function of the first kind. In the parallel limit $\alpha \rightarrow 0$, we find an analytical expression for \mathcal{F}_{PS} :

$$\mathcal{F}_{\text{PS}}(r, \alpha \rightarrow 0) = \frac{1}{2 + \kappa_0^2 r^2} \left\{ 1 + e^{-2\kappa_0^2 r^2} \left[(1 + \kappa_0^2 r^2) \cos(2\sqrt{2}\kappa_0 r) - \frac{\kappa_0 r}{\sqrt{2}} \sin(2\sqrt{2}\kappa_0 r) \right] \right\}. \quad (4.11)$$

The de Broglie wavelength of the axion DM is given by $\lambda_{\text{dB}} \sim 1/\kappa_0$. For $r \ll 1/\kappa_0$, there is $\mathcal{F}_{\text{PS}} \rightarrow 1$, and we recover the result in the coherent limit as expected. On the other hand, for $r \gg 1/\kappa_0$, Eq. (4.11) is reduced to

$$\mathcal{F}_{\text{PS}}(r \gg \kappa_0^{-1}, \alpha \rightarrow 0) = 1/(\kappa_0^2 r^2). \quad (4.12)$$

So, the phase-space decoherence effect causes a quadratic suppression of the axion force at long distances.

For a generic value of α , the integral in Eq. (4.10) can only be calculated numerically. In the left panel of Fig. 4, we show \mathcal{F}_{PS} as a function of r for $\alpha = 0, 30^\circ, 45^\circ, 60^\circ$ and 90° . In the coherent limit $r \ll 1/\kappa_0$, $\mathcal{F}_{\text{PS}} \rightarrow 1$ for any value of α . The distinguishable effects from different angles start to appear in the non-coherent region. For $\alpha \in [0, 45^\circ)$, \mathcal{F}_{PS} is positive across all distances and scales as $1/r^2$ at $r \gg 1/\kappa_0$, and \mathcal{F}_{PS} decreases monotonically as one increases α ; when α is around 45° , there is partial cancellation happening between the two terms in Eq. (2.26) after the phase-space integral, making \mathcal{F}_{PS} more suppressed and scaling as $1/r^4$; for $\alpha \in (45^\circ, 90^\circ]$, \mathcal{F}_{PS} changes sign around $r \sim 1/\kappa_0$ and again scales as $1/r^2$ at $r \gg 1/\kappa_0$, and $|\mathcal{F}_{\text{PS}}|$ increases monotonically when α varies from 45° to 90° .

In the right panel of Fig. 4, we make the contour plot of \mathcal{F}_{PS} with different values of r and α . The contour lines also indicate that $|\mathcal{F}_{\text{PS}}|$ attains its lowest around $\alpha = 45^\circ$ and $\alpha = 135^\circ$. Clearly, \mathcal{F}_{PS} is symmetric under the transformation $\alpha \rightarrow \pi - \alpha$, as also implied by Eq. (4.10). This can be understood in the following way: although the axion DM wind

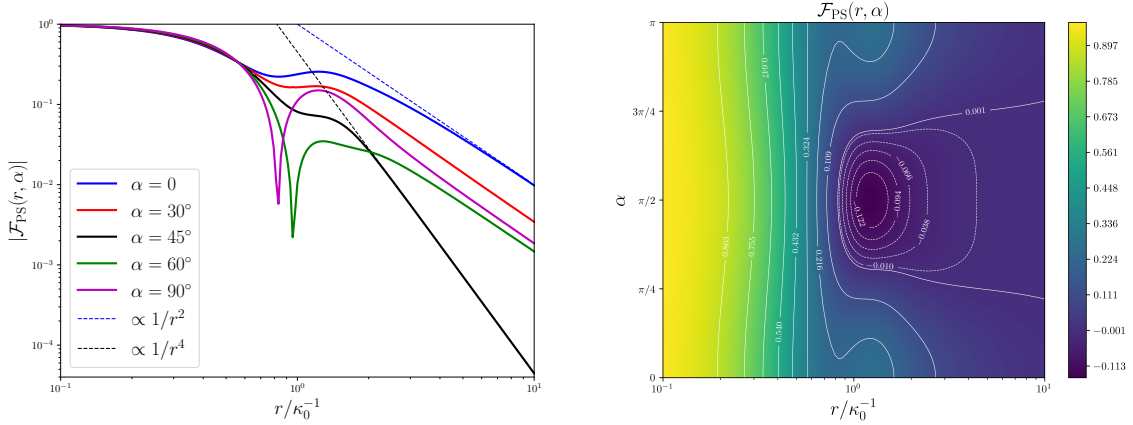


Figure 4. The phase-space form factor \mathcal{F}_{PS} . *Left panel:* the scaling behavior of the magnitude of \mathcal{F}_{PS} with r for different values of α . Note the cusps correspond to the place where \mathcal{F}_{PS} changes sign. *Right panel:* the contour plot of \mathcal{F}_{PS} as a function of r and α .

picks a preferred direction by \mathbf{v}_a , there is no net momentum transfer between the two-object system and the axion background — ψ_1 borrows some momentum from the background but ψ_2 returns the same momentum back to the background, and vice versa (see Fig. 2). As a result, the magnitude of the background-induced force from object 1 to object 2 should be equal to that from object 2 to object 1 according to the momentum conservation. Therefore, the \mathbb{Z}_2 symmetry is kept at the potential level: $V_{\text{bkg}}(\mathbf{r}) = V_{\text{bkg}}(-\mathbf{r})$. Since $V_{\text{bkg}} \propto \mathcal{F}_{\text{PS}}$, the form factor is also invariant under reflection.

In conclusion, the above decoherence effect from phase-space spread is crucial to consider in the detection of axion DM, which may decrease the sensitivity compared to the coherent limit. In particular, the different scaling behavior between $\alpha \approx 45^\circ$ and the other values of α provides an interesting possibility to probe the periodic and time-varying signals due to the Earth’s motion relative to the axion DM wind.

Finite-size object

In actual fifth-force detection experiments, the object has a finite size. We simplify the geometric setup by treating the target as a point-like object while the source is a ball with radius R and constant density (this corresponds to the MICROSCOPE-like experiments). We choose the center of the ball as the reference point and denote the vector from the center of the ball to the point-like object as \mathbf{r} with $r \equiv |\mathbf{r}| > R$, as shown in Fig. 5. Then the background-induced axion forces between them turn out to be

$$V_{\text{bkg,ball}}^{\text{shft}}(\mathbf{r}; \mu) = -\frac{\mu^2 \rho_a}{4\pi f_a^4 m_a^2} \frac{N_p N_b}{V_b} \int_{\text{ball}} d^3 \mathbf{r}' \frac{\mathcal{F}_{\text{PS}}(\mathbf{r} - \mathbf{r}')}{|\mathbf{r} - \mathbf{r}'|}, \quad (4.13)$$

$$V_{\text{bkg,ball}}^{\text{inv}}(\mathbf{r}) = -\frac{c_N^4 \rho_a m_a^2}{64\pi f_a^4 m_N^2} \frac{N_p N_b}{V_b} \int_{\text{ball}} d^3 \mathbf{r}' \frac{\mathcal{F}_{\text{PS}}(\mathbf{r} - \mathbf{r}')}{|\mathbf{r} - \mathbf{r}'|}, \quad (4.14)$$

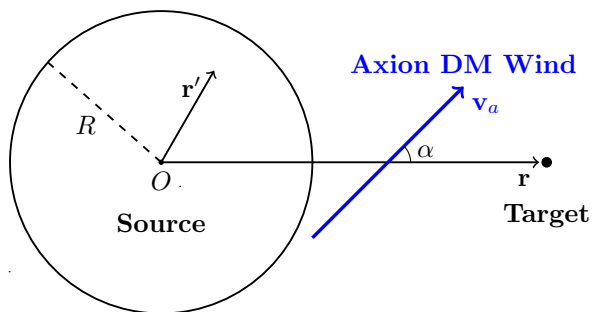


Figure 5. The schematic plot of the axion force in the background of the axion DM wind between a finite-size source and a point-like target.

where N_p and N_b are the number of nucleons in the point-like object and the ball, respectively, and $V_b = 4\pi R^3/3$ is the volume of the ball. The physical observable in the fifth-force experiments is proportional to the correction to gravity: $\delta V/V_{\text{grav}}$. Comparing the axion forces with gravity, one obtains

$$\frac{\delta V_{\mu\text{-term}}}{V_{\text{grav}}} = \frac{2\mu^2 \rho_a M_{\text{Pl}}^2}{f_a^4 m_a^2 m_N^2} \mathcal{F}_{\text{tot}} , \quad (4.15)$$

$$\frac{\delta V_{\text{mass-term}}}{V_{\text{grav}}} = \frac{c_N^4 \rho_a m_a^2 M_{\text{Pl}}^2}{8f_a^4 m_N^2} \mathcal{F}_{\text{tot}} , \quad (4.16)$$

where \mathcal{F}_{tot} is the total form factor that includes the decoherence effect from both phase space and the finite size:

$$\mathcal{F}_{\text{tot}}(\mathbf{r}) \equiv \frac{r}{V_b} \int_{\text{ball}} d^3\mathbf{r}' \frac{\mathcal{F}_{\text{PS}}(\mathbf{r} - \mathbf{r}')}{|\mathbf{r} - \mathbf{r}'|} . \quad (4.17)$$

\mathcal{F}_{tot} can be calculated numerically using Eqs. (F.8)-(F.9) and (4.10).

In Fig. 6, we show the scaling behavior of \mathcal{F}_{tot} for different sizes of the object: $r = 1.1R$, $r = 2R$, $r = 3R$ and $r = 10R$. The result of \mathcal{F}_{tot} with $r = 10R$ already agrees well with that of \mathcal{F}_{PS} , so $r = 10R$ can be taken as the point-source limit, where the finite-size effect is irrelevant. For larger objects, we find that the finite-size effect does not change the scaling behavior of the axion force as long as $\alpha \neq 45^\circ$. For example, the source with $r = 1.1R$ only decreases \mathcal{F}_{tot} by about a factor of 2 compared to the point-source limit for $\alpha = 0$, as shown in the left panel of Fig. 6. However, the finite-size effect becomes important when α is close to 45° . This is because at long distances $r \gg R$, the partial cancellation still exists and leads to $\mathcal{F}_{\text{tot}} \propto 1/r^4$, similar to the point-source limit, but as the target gets closer to the source, the cancellation no longer occurs for most of the points in the source, for which the effective angle is away from 45° . As a result, the finite size enhances \mathcal{F}_{tot} compared to the point-source limit and makes it again scale as $1/r^2$. This is shown in the right panel of Fig. 6.

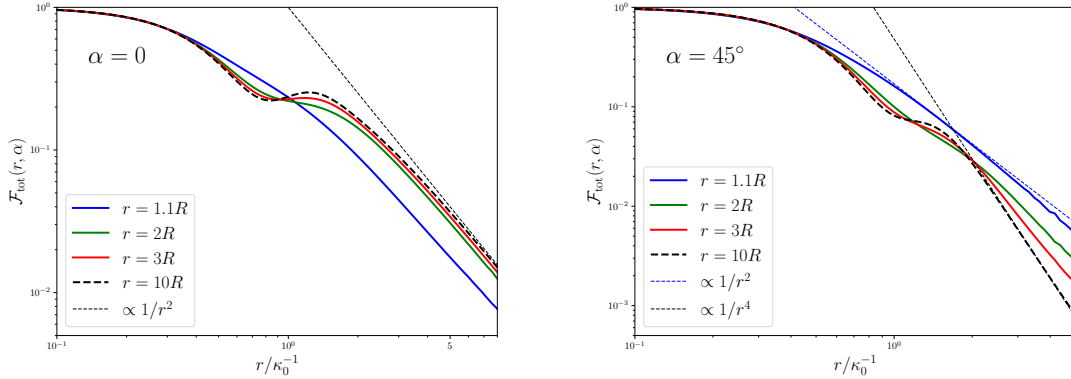


Figure 6. The scaling behavior of the total form factor \mathcal{F}_{tot} from a finite-size object with a radius R at $\alpha = 0$ (left) or $\alpha = 45^\circ$ (right). The thick black dashed lines ($r = 10R$) correspond to the point-object limit.

4.1.3 Fifth-force bounds

Then we calculate the experimental bounds on the axion couplings from the fifth-force searches for the axion forces. We map Eqs. (4.15)-(4.16) to the experimental sensitivities in Tab. 2, taking into account the decoherence effect from \mathcal{F}_{tot} in Eq. (4.17). For concreteness, we take $\alpha = 0$ to maximize the background effect and fix $r = 1.1R$ (corresponding to the setup of MICROSCOPE [64]).

The results are shown in Fig. 7 and Fig. 8. We plot the bounds separately from the background-induced axion force V_{bkg} (solid lines) and the vacuum two-axion force V_{2a} (dashed lines). For V_{bkg} , we fix $\rho_a = \rho_{\text{DM}} = 0.4 \text{ GeV}/\text{cm}^3$. Note that for $m_a \ll \text{GeV}$, the contribution to V_{bkg} from the mass term (4.16) is negligible compared to that from the μ -term (4.15). The bounds from V_{2a} remain constant in the small axion mass limit, but the sensitivities decrease exponentially when the axion mass is greater than the inverse of the experimental length scale, as indicated by Eq. (2.33). On the other hand, for a fixed energy density, the sensitivity of the bounds from V_{bkg} is enhanced for smaller axion masses due to the increasing occupation number of background axions. However, from a theoretical point of view, the sensitivity cannot increase infinitely by keeping decreasing the axion mass, otherwise the axion classical field value is too large to invalidate the axion effective coupling in Eq. (2.29). As a conservative bound, the axion field value cannot exceed the cutoff scale f_a — this corresponds to the purple dashed line in Fig. 7, above which the contributions from higher-order axion couplings might be relevant. When the experimental length scale is greater than the de Broglie wavelength of the background axions $\lambda_{\text{dB}} \sim 10^3/m_a$, the sensitivities are additionally reduced by the decoherent effects from \mathcal{F}_{tot} , which corresponds to the turning points of the solid lines in Figs. 7 and 8. In most of the parameter space, the contribution from V_{bkg} by assuming an axion DM background dominates over that from V_{2a} . It can be seen from Fig. 7 that for axion DM lighter than about 10^{-9}eV , and when the effective coupling μ is not much more

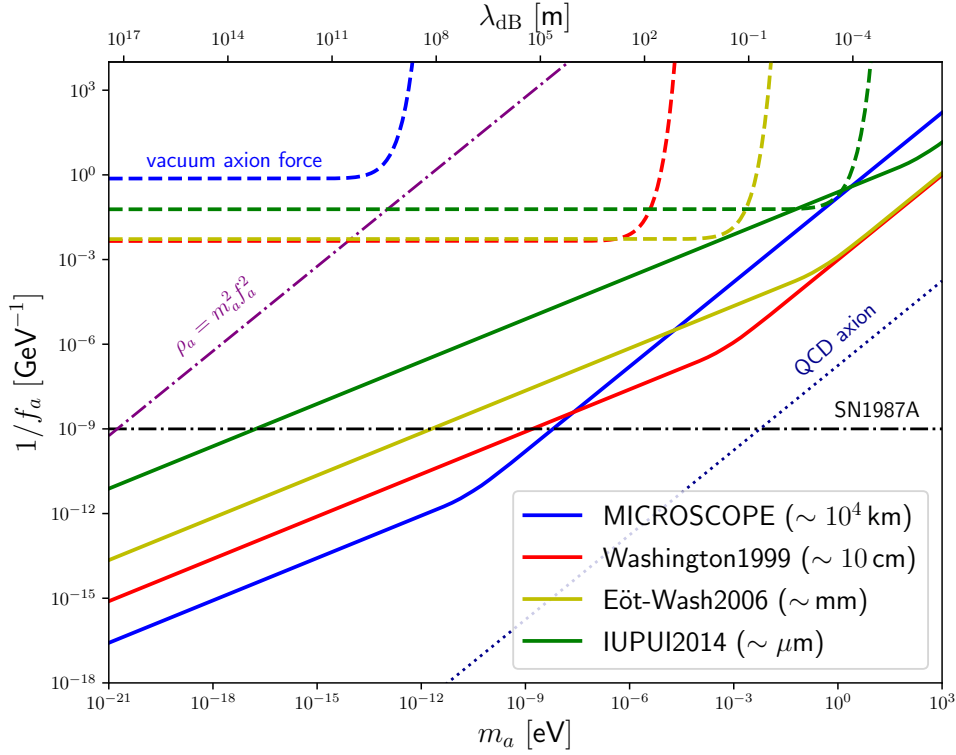


Figure 7. Fifth-force bounds on the axion couplings from the axion forces. The solid lines correspond to the search for the axion force induced from the axion DM background V_{bkg} by fixing $\rho_a = \rho_{\text{DM}} = 0.4 \text{ GeV/cm}^3$ and $\mu = \mu_{\text{QCD}} = 15 \text{ MeV}$, where different colors denote the experiments at different length scales. The purple dash-dotted line corresponds to the effective theory bound in Eq. (2.42), above which the correction to V_{bkg} from axion self-interactions might be non-negligible. The dashed lines with different colors correspond to the search for the vacuum two-axion force V_{2a} by assuming $\rho_a = 0$. The black dash-dotted line denotes the generic astrophysical bound $f_a \gtrsim 10^9 \text{ GeV}$ [89–92]. The dark-blue dotted line corresponds to the relation of QCD axion: $m_a f_a \approx 5.7 \times 10^{-3} \text{ GeV}^2$ [77].

suppressed compared to μ_{QCD} , the bound from V_{bkg} is stronger than the existing astrophysical bound $f_a \gtrsim 10^9 \text{ GeV}$.

In Fig. 9, we show the bounds for heavier axions with $\text{keV} < m_a < \text{GeV}$. In this region, the astrophysical constraints are largely relaxed. The vacuum axion force has a very short range and thus is totally negligible in the practical fifth-force experiments. On the other hand, V_{bkg} is only quadratically suppressed due to the decoherence effect: $\mathcal{F}_{\text{tot}} \propto 1/(m_a^2 r^2)$, where r is the experimental length scale. In the heavy axion mass region, the contribution to V_{bkg} from the mass term (4.16) is non-negligible and is shown with dash-dotted lines (with $c_N = 1$) in Fig. 9. The contribution from the μ -term (4.15) is shown with dotted lines, and the solid lines represent the combined effects.

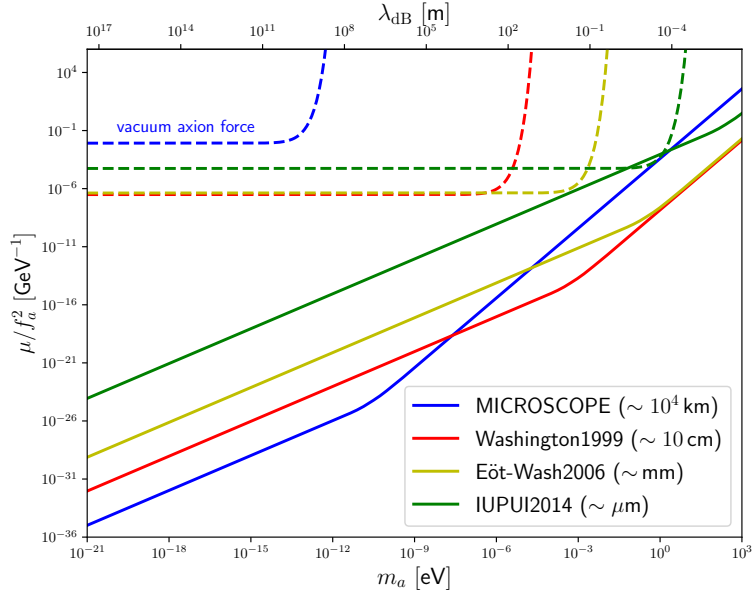


Figure 8. Same conventions as Fig. 7, but with μ as a free parameter.

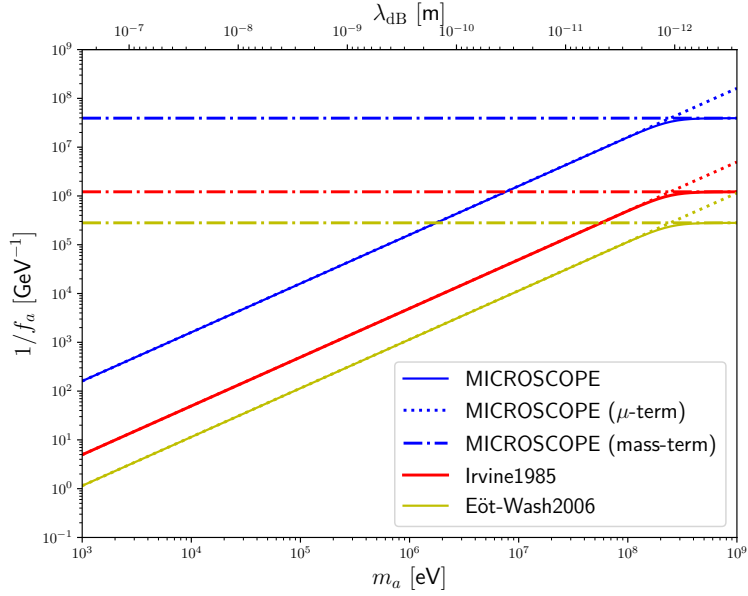


Figure 9. Same conventions as Fig. 7 but in the heavy axion mass region, where the astrophysical bound is relaxed. The dotted (dash-dotted) lines correspond to the contribution to V_{bkg} from μ -term (mass term), while the solid lines include both contributions.

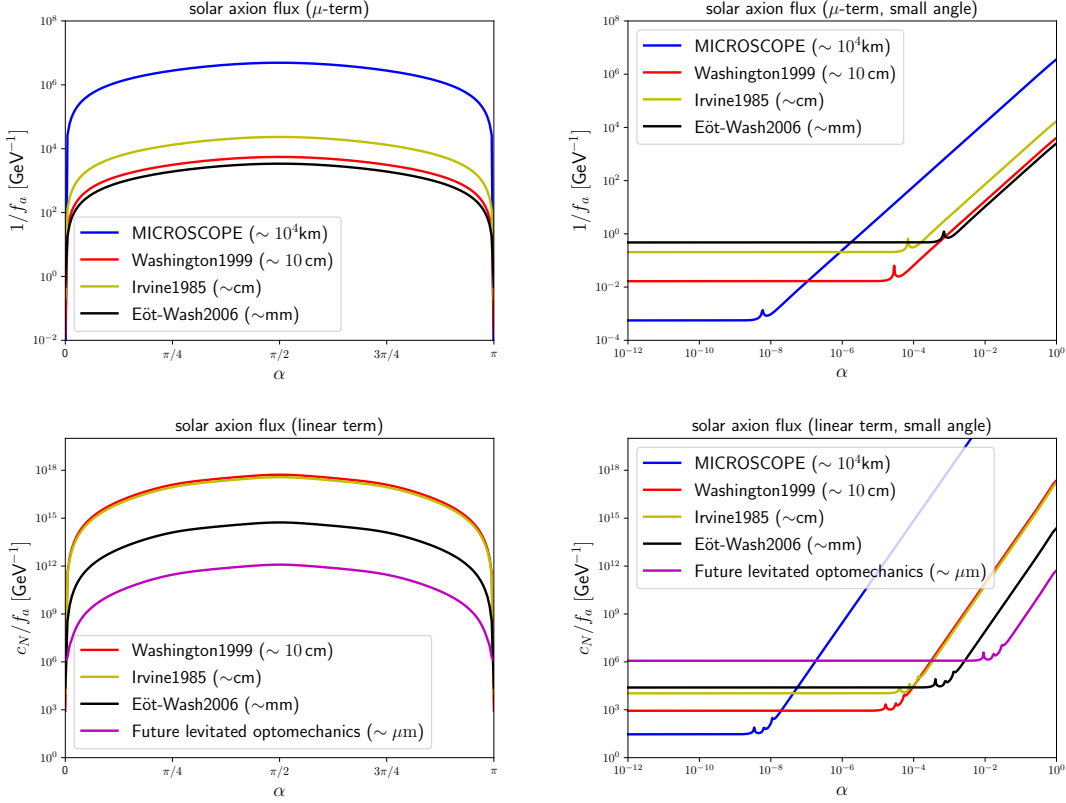


Figure 10. Constraints on the axion coupling from the axion force induced by the solar axion flux. The bounds are applicable for relativistic solar axions ($m_a \ll \text{keV}$). The diagrams in the first line and second line correspond to the axion force in Eq. (3.15) with $\mu = \mu_{\text{QCD}}$ and that in Eq. (3.16) with $c_1 = c_2 = c_N$ and $m_1 = m_2 = m_N$, respectively. The sensitivities and length scales of specific experiments are taken from Tab. 2. In the left panel, we show the constraints for $\alpha \in [0, \pi)$, while the right panel zooms in the constraints at small values of the angle (coherent limit). The cusps correspond to the places where the axion forces change the sign.

4.2 Solar axion flux

The Sun is another typical source of axion background. Axions can be copiously produced in the Sun through their coupling to photons $\mathcal{L} \supset -g_{a\gamma\gamma} a F \tilde{F} / 4$, via the Primakoff process [93]: $\gamma + \psi \rightarrow a + \psi$. Here γ is a photon, F and \tilde{F} are the electromagnetic tensor and its dual, respectively, and ψ is a charged particle.

The first semi-analytical spectrum for solar axion flux was derived in [94], where the typical energy scale is $\kappa_0 \sim \mathcal{O}(\text{keV})$. For the practical calculation in this work, we use the solar axion spectrum fitted by the CAST collaboration [57]:

$$\frac{d\Phi}{d\kappa} = 6.02 \times 10^{10} \text{ cm}^{-2} \text{ s}^{-1} \text{ keV}^{-1} \left(\frac{g_{a\gamma\gamma}}{10^{-10} \text{ GeV}^{-1}} \right)^2 \left(\frac{\kappa}{\text{keV}} \right)^{2.481} \exp\left(-\frac{\kappa}{1.205 \text{ keV}} \right). \quad (4.18)$$

The spectrum in Eq. (4.18) is valid for relativistic axions (i.e., $m_a \ll \text{keV}$), see [95] for the correction of the spectrum from the axion mass. In the following, we take $g_{a\gamma\gamma} = 10^{-10} \text{ GeV}^{-1}$ to saturate the CAST bound on the axion-photon coupling and investigate the constraints on the axion-nucleon coupling from fifth-force experiments.

The general expression of the axion force in the background of a relativistic axion flux has been derived in Eqs. (3.15)-(3.16). Substituting the spectrum (4.18) into Eqs. (3.15)-(3.16) and performing the integral, we obtain the axion force induced by the solar axion background. The calculation details are provided in App. G, and the constraints are plotted in Fig. 10.

Sensitivities are enhanced in the small- α limit, where all axions in the flux can coherently contribute to V_{bkg} . When $\alpha^2 \gtrsim \kappa_0 r \sim (r/0.1 \text{ nm})$, the decoherence effect starts to appear and sensitivities are decreased, corresponding to the turning points of the curves in the right panel of Fig. 10. For $\alpha^2 \gg \kappa_0 r$, sensitivities are suppressed by some inverse power of $(r/0.1 \text{ nm})$ [see Eqs. (G.7)-(G.8) for detailed expressions] compared to the coherent limit, where r is the length scale of the experiment.

From Fig. 10, we conclude that the fifth-force bound from the solar axion flux is much weaker than the astrophysics bound. Even in the most optimistic case (coherent limit), the best constraint is $f_a \gtrsim 10^3 \text{ GeV}$.

4.3 Atomic spectroscopy

Over the last two decades, significant advancements in quantum technology have rendered precision atomic physics a promising approach to probe new physics at low-energy scales (see [96] for a review). Atomic systems usually have better sensitivities compared to the traditional experiments at macroscopic scales to search for the fifth force and are particularly useful to probe the interactions mediated by particles that couple feebly to ordinary matter. For example, a long-range spin-spin interaction can lead to a hyperfine splitting in the atomic ground state, which has been precisely measured [97–99]. Moreover, any interaction that fundamentally violates parity can contribute to atomic parity violation, an observable that has been well measured in Cesium [100–102]. The utilization of atomic systems for detecting the long-range force mediated by neutrinos was recently discussed in [103–106].

In this work, we are interested in the spin-independent axion force induced by an axion background, which does not contribute to hyperfine splitting or atomic parity violation. However, the spin-independent axion force is coherent in the sense that its magnitude is proportional to the number of nucleons in atoms coupled to the axion. As a result, it contributes differently in atoms with different numbers of nucleons and can be probed by the atomic isotope shift [107].

As a simple example, we use the $1S - 2S$ isotope shift measured in the Hydrogen-Deuterium system [108]:

$$\Delta\nu_{\text{exp}} \equiv \nu_{1S-2S}^{\text{D}} - \nu_{1S-2S}^{\text{H}} - \Delta\nu_{\text{HFS}} = 670994334606(15) \text{ Hz} , \quad (4.19)$$

where ν_{1S-2S}^D and ν_{1S-2S}^H denote the transition frequency between $1S$ and $2S$ states in Deuterium and Hydrogen, respectively, and $\Delta\nu_{\text{HFS}}$ is the hyperfine structure correction. Note that the spin-independent axion force does not contribute to $\Delta\nu_{\text{HFS}}$. On the other hand, the theoretical prediction from the Standard Model interaction reads [108]:

$$\Delta\nu_{\text{th}} = 670999566.90(66)(60) \text{ kHz} . \quad (4.20)$$

Combining Eqs. (4.19) and (4.20) we have

$$|\delta\nu_{\text{HD}}| \equiv |\Delta\nu_{\text{exp}} - \Delta\nu_{\text{th}}| \approx 5.2 \text{ MHz} \approx 2.2 \times 10^{-8} \text{ eV} . \quad (4.21)$$

As a conservative limit, the contribution from axion forces should not exceed Eq. (4.21).

In the following, we calculate the axion contribution to the isotope shift in the Hydrogen-Deuterium system. We assume that axions comprise DM and that the axion force is dominated by the quadratic coupling in Eq. (2.29). We include contributions from both the background-induced axion force V_{bkg} and the vacuum two-axion force V_{2a} . Note that the tree-level axion force in Eq. (A.6) does not contribute because the tensor structure vanishes for S -state matrix elements:

$$\left\langle nS \left| \frac{3(\boldsymbol{\sigma}_e \cdot \hat{\mathbf{r}})(\boldsymbol{\sigma}_N \cdot \hat{\mathbf{r}}) - (\boldsymbol{\sigma}_e \cdot \boldsymbol{\sigma}_N)}{r^3} \right| nS \right\rangle \equiv 0 , \quad (4.22)$$

where n is any positive integer, $\boldsymbol{\sigma}_e$ and $\boldsymbol{\sigma}_N$ are the spin operators of the electron and the nucleon in the atom.

For the sub-eV axion DM, its de Broglie wavelength $\lambda_{\text{dB}} \sim 0.02 \text{ cm}$ (eV/m_a) is much larger than the atomic length scale. As a result, it is an extremely good approximation to take the coherent limit. Using Eq. (2.41), the background-induced axion force between the electron and the nucleon reads

$$V_{\text{bkg}}^{eN}(r) = -\frac{\mu_e \mu_N \rho_a}{4\pi r f_a^4 m_a^2} , \quad (4.23)$$

where μ_e and μ_N correspond to the quadratic coupling in Eq. (2.29) with ψ replaced by the electron or the nucleon, respectively. It is straightforward to calculate the induced matrix elements:

$$\left\langle nS \left| V_{\text{bkg}}^{eN} \right| nS \right\rangle = -\frac{\mu_e \mu_N \rho_a}{4\pi f_a^4 m_a^2 a_0 n^2} , \quad (4.24)$$

where $a_0 \approx 1/(3.7 \text{ keV})$ is the Bohr radius.

On the other hand, the vacuum two-axion force V_{2a}^{eN} is given by Eq. (2.31) with $\mu^2 \rightarrow \mu_e \mu_N$. However, since $V_{2a}^{eN} \propto 1/r^3$ at short distances, the S -state matrix elements induced by V_{2a}^{eN} are divergent, indicating the failure of the effective coupling (2.29) at high-energy scales. To estimate the effect from the vacuum two-axion force, we put a cutoff at $r = 1/f_a$

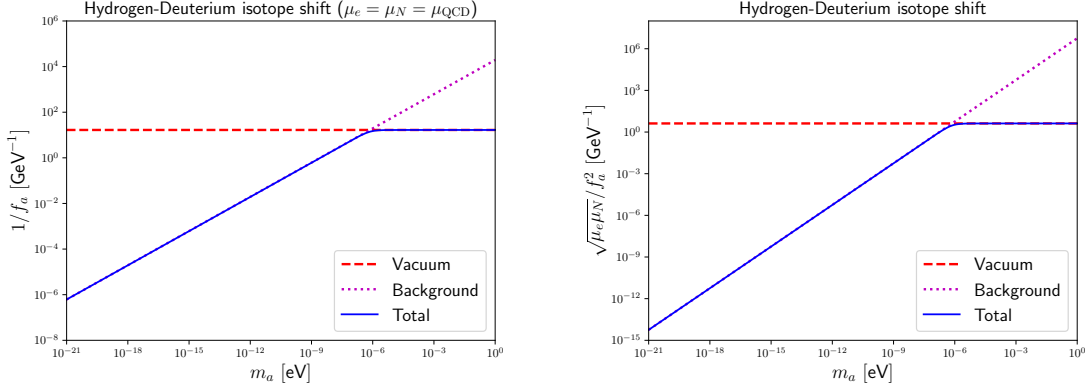


Figure 11. Constraints on the axion coupling from the isotope shift measured in the Hydrogen-Deuterium system. The dashed lines and the dotted lines correspond to the contribution from the vacuum two-axion force V_{2a} and the background-induced axion force V_{bkg} (with $\rho_a = \rho_{\text{DM}} = 0.4 \text{ GeV}/\text{cm}^3$ fixed), respectively, while the solid lines include both contributions. In the left panel we fix $\mu_e = \mu_N = \mu_{\text{QCD}} = 15 \text{ MeV}$ and put the bound on $1/f_a$; in the right panel we take μ_e and μ_N as free parameters and put the model-independent bound on $\sqrt{\mu_e \mu_N}/f_a^2$.

in the radial integral, leading to

$$\begin{aligned} \langle 1S | V_{2a}^{eN} | 1S \rangle &= -\frac{\mu_e \mu_N m_a}{8\pi^3 f_a^4 a_0^3} \int_{1/f_a}^{\infty} dr K_1(2m_a r) e^{-2r/a_0} \\ &\approx -\frac{\mu_e \mu_N}{16\pi^3 f_a^4 a_0^3} \left[\log\left(\frac{f_a a_0}{2}\right) - \gamma_E \right] + \mathcal{O}\left(\frac{1}{f_a a_0}\right), \end{aligned} \quad (4.25)$$

$$\begin{aligned} \langle 2S | V_{2a}^{eN} | 2S \rangle &= -\frac{\mu_e \mu_N m_a}{256\pi^3 f_a^4 a_0^3} \int_{1/f_a}^{\infty} dr K_1(2m_a r) \left(2 - \frac{r}{a_0}\right)^2 e^{-r/a_0} \\ &\approx -\frac{\mu_e \mu_N}{128\pi^3 f_a^4 a_0^3} \left[\log(f_a a_0) - \gamma_E - \frac{3}{2} \right] + \mathcal{O}\left(\frac{1}{f_a a_0}\right), \end{aligned} \quad (4.26)$$

where $\gamma_E \approx 0.577$ is Euler's constant. Note that in the second line of Eqs. (4.25) and (4.26), we have assumed $f_a \gg 1/a_0 \approx 3.7 \text{ keV}$; in this case, the matrix elements only depend logarithmically on the cutoff scale.

Combining Eqs. (4.24)-(4.26), we obtain the isotope shift in the Hydrogen-Deuterium system caused by the axion force:

$$\delta\nu_{\text{axion}} \approx \frac{3\mu_e \mu_N \rho_a}{16\pi f_a^4 m_a^2 a_0} + \frac{7\mu_e \mu_N}{128\pi^3 f_a^4 a_0^3} \left[\log(f_a a_0) + \frac{3}{14} - \gamma_E - \frac{8}{7} \log 2 \right], \quad (4.27)$$

where we have neglected the difference between protons and neutrons and assumed both of their couplings to the axion are described by μ_N . The first (second) term in Eq. (4.27) corresponds to the contribution from V_{bkg} (V_{2a}). To get a bound on the axion coupling, we assume that there are no new-physics contributions to the isotope shift other than the axion

force and ask $|\delta\nu_{\text{axion}}| \leq |\delta\nu_{\text{HD}}|$. The corresponding bound is shown in Fig. 11.

In addition to the isotope shift, the axion force can also contribute to the $1S - 2S$ transition frequency of non-hadronic atoms such as muonium (if axions couple to charged leptons), which has been measured with high precision [109]. The ongoing Mu-MASS experiment could further improve the sensitivity of the measurement of the muonium $1S - 2S$ transition frequency by three orders of magnitude [110].

5 Comparison with the literature

The detection of light DM using background effects has attracted a great deal of attention in recent years. In this regard, it is useful to compare our results with those in the literature.

The background-induced force mediated by quadratically coupled scalars was first calculated in [54, 55], which assumed a thermal distribution of background scalars. Recently, the formalism was generalized to an arbitrary non-thermal background in [42, 43] and was applied to the detection of light mediators by assuming they form a non-relativistic DM background. The background-induced axion force V_{bkg} calculated in this work includes both linear and quadratic couplings, as well as the relativistic correction from axion backgrounds. In particular, we find that the result of V_{bkg} induced by a pure quadratic coupling in the non-relativistic limit agrees with the scalar case calculated in [42, 43].

The decoherence effect on the background-induced force from DM phase-space spread was studied in [42], using an asymmetric decoherence factor $\mathcal{D}_{\text{asy}} = \cos(|\mathbf{k}|r - \mathbf{k} \cdot \mathbf{r})$ that comes from the retarded propagator. In this work, we derived a symmetric decoherence factor $\mathcal{D} = [\cos(|\mathbf{k}|r - \mathbf{k} \cdot \mathbf{r}) + \cos(|\mathbf{k}|r + \mathbf{k} \cdot \mathbf{r})]/2$ by explicitly computing the scattering amplitudes mediated by two axions using the Feynman propagator. Our result agrees with that of [42] in both the isotropic limit and the coherent limit; in the decoherent region with anisotropic backgrounds, our phase-space form factor shares a similar quadratic suppression $\mathcal{F}_{\text{PS}} \propto \lambda_{\text{dB}}^2/r^2$ as that in [42] but differs by an $\mathcal{O}(1)$ numerical factor. In addition to the phase-space suppression, we also explicitly calculated the decoherence effect from the finite-size spread of the object. We find that finite-size effects do not change the scaling behavior of the axion force in the general case.

All the formalisms adopted in [42, 43, 54, 55] as well as in this work used quantum field theories to compute the relevant scattering amplitudes and then mapped them onto the non-relativistic potential. However, the background effect can also be captured by performing a pure quantum-mechanical-like calculation and solving the scalar equation of motion with fixed boundary conditions [20, 37, 45, 50]. Our result of V_{bkg} induced by a pure quadratic coupling agrees with their results in the coherent region.

Finally, we comment on the possible influence of the matter effect on the axion force. When deriving the experimental bounds in Sec. 4.1, we have fixed the energy density of the axion background to be the DM density in the galaxy, $\rho_a = \rho_{\text{DM}} \approx 0.4 \text{ GeV}/\text{cm}^3$, that is, we assumed the axion field value on the surface of the Earth the same as the average value in the galaxy. However, this might not be the case because the matter effect of Earth may

change the axion field value around the Earth as well as its spatial gradient through the axion coupling to ordinary matter, as recently pointed out in [48, 49] (see also [44, 45]). The effective axion density around the Earth is then shifted: $\rho_a \rightarrow \rho_a^{\text{eff}}$, so is its gradient. Note that the physical observables induced by the axion force depend on both the axion field value and its spatial gradient. As a result, the bounds derived in Sec. 4.1 in the strongly coupled (i.e., small f_a) region may be modified by the Earth matter effect in a nontrivial way. We leave the detailed analysis for future studies.

6 Conclusions

In this work, we studied the spin-independent force mediated by two axions in the presence of an axion background, which is the leading long-range coherent effect caused by axions.

We started from the effective axion interactions including both linear and quadratic couplings to the SM fermions and derived a general expression for the background-induced axion force V_{bkg} , which is applicable to arbitrary axion backgrounds. We find that the magnitude of this force is controlled by the degree of shift symmetry breaking. There are three relevant effects to break the shift symmetry. First, the axion mass behaves as an order parameter that breaks the shift symmetry and leads to a nonzero V_{bkg} , but this effect is suppressed for light axions. Going beyond the mass term, the shift symmetry is explicitly broken by the axion quadratic coupling to SM fermions, whose magnitude can be much larger than the axion mass and results in a significant enhancement to V_{bkg} . In the absence of quadratic coupling, the shift symmetry is also effectively broken by the axion background, which is essentially the relativistic correction to the NR amplitude; in an energetic axion background, this effect dominates over the axion mass contribution and enhances V_{bkg} .

In the presence of shift symmetry breaking, V_{bkg} has a generic $1/r$ scaling behavior as long as $r \ll \lambda_{\text{dB}}$, the de Broglie wavelength of the background axions. Moreover, V_{bkg} is proportional to the number density of background axions, indicating that particles within the volume of λ_{dB}^3 coherently contribute to V_{bkg} . This is a significant effect if axions are cold DM that has a huge occupation number. At distances $r \gtrsim \lambda_{\text{dB}}$, the background axions generically have different phases and thus contribute destructively to V_{bkg} , making it more suppressed than $1/r$. We calculated this effect with a symmetric decoherence factor by including the finite spread from both the phase space and the configuration space. We find that for most realistic axion backgrounds, the suppression is some power of λ_{dB}/r , as opposed to an exponential suppression $e^{-2m_a r}$ to the vacuum two-axion force V_{2a} . This reflects the intrinsic difference between the quantum force and the background-induced force: V_{2a} is a pure quantum effect, where both propagators are off-shell; this effect is exponentially suppressed when the distance exceeds the inverse mass of the propagator. On the other hand, V_{bkg} is essentially a classical effect since one of the propagators is on-shell; the scattering between external particles and background particles extends the range of this effect, allowing it to go much further than the inverse mass of the propagator. As a result, V_{bkg} is much more significant on macroscopic length scales compared to its vacuum counterpart V_{2a} .

The background-induced axion force has rich phenomena given that axion backgrounds exist in a large class of well-motivated scenarios. We calculated its effect in fifth-force detection experiments by separately assuming the existence of axion DM background and solar axion flux. We find that the effect induced from the DM background of ultralight axions could be strong enough to exceed the existing astrophysical bound. The axion force can also cause an energy shift for the atomic states and can be probed using atomic spectroscopy, which is a promising method with sensitivities that will be significantly improved in the near future. Another interesting application that is not discussed in this work is to investigate the effect of this long-range force at galactic scales in the early universe — this effect is expected to be significant because the axion DM number density is much higher in the early universe than at present.

In conclusion, our results demonstrate that the background effect could be very important for detecting axions and axion DM, and would also be helpful in searching for other exotic light particles beyond the SM.

Acknowledgement

We would like to thank Abhishek Banerjee, Sergio Barbosa, Itay Bloch, Jeff Dror, Francesc Ferrer, Sylvain Fichet, Xucheng Gan, Anson Hook, Da Liu, Di Liu, Xuheng Luo, Maxim Perelstein, and Ken Van Tilburg for helpful discussions. We thank Itay Bloch and Maxim Perelstein for insightful comments on the draft. We thank Sergio Barbosa, Sylvain Fichet, and Ken Van Tilburg for discussions on the form of the decoherence factor. We thank Xucheng Gan and Xuheng Luo for discussions on the finite-size decoherence effect. This work is supported in part by the NSF grant PHY-2309456.

A Axion forces at the tree level

Although we focus on the two-axion forces throughout this work, we would like to briefly review the one-axion effect in this appendix, which, as we show below, is always spin-dependent due to the pseudoscalar nature of the coupling.

The linear coupling between the axion and fermions in Eq. (2.2) leads to tree-level t -channel scattering $\psi_1(p_1) + \psi_2(p_2) \rightarrow \psi_1(p'_1) + \psi_2(p'_2)$ by exchanging one axion (see Fig. 12). The amplitude reads

$$i\mathcal{M}_{\text{tree}} = \frac{c_1 c_2}{4f_a^2} \bar{u}(p'_1) \not{q} \gamma_5 u(p_1) \bar{u}(p'_2) \not{q} \gamma_5 u(p_2) \frac{i}{q^2 - m_a^2}, \quad (\text{A.1})$$

where $c_i \equiv c_{\psi_i}$ (for $i = 1, 2$) and $u(p)$ denotes the wavefunction of external fermions with momentum p . Using the equation of motion of external fermions, it is reduced to

$$\mathcal{M}_{\text{tree}} = -\frac{c_1 c_2 (2m_1)(2m_2)}{4f_a^2 (q^2 - m_a^2)} [\bar{u}(p'_1) \gamma_5 u(p_1)] [\bar{u}(p'_2) \gamma_5 u(p_2)]. \quad (\text{A.2})$$

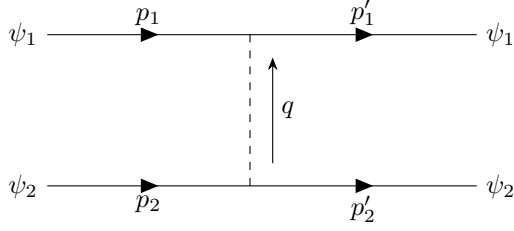


Figure 12. The Feynman diagram of one-axion exchange between two fermions.

Under the NR approximation $q^\mu \approx (0, \mathbf{q})$, we have

$$\bar{u}(p'_1)\gamma_5 u(p_1) = \boldsymbol{\sigma}_1 \cdot \mathbf{q} + \mathcal{O}(\mathbf{q}^2), \quad \bar{u}(p'_2)\gamma_5 u(p_2) = -\boldsymbol{\sigma}_2 \cdot \mathbf{q} + \mathcal{O}(\mathbf{q}^2), \quad (\text{A.3})$$

where $\boldsymbol{\sigma}_i \equiv \xi_i^\dagger \boldsymbol{\sigma} \xi_i$ (for $i = 1, 2$) has been defined, $\boldsymbol{\sigma} = (\sigma_1, \sigma_2, \sigma_3)$ is the vector of Pauli matrices, and ξ_i denotes the two-component spinor of ψ_i that satisfies the Dirac equation. This leads to the NR amplitude:

$$\frac{\mathcal{M}_{\text{tree,NR}}}{(2m_1)(2m_2)} = \frac{c_1 c_2}{4f_a^2} \frac{1}{\mathbf{q}^2 + m_a^2} (\boldsymbol{\sigma}_1 \cdot \mathbf{q}) (\boldsymbol{\sigma}_2 \cdot \mathbf{q}). \quad (\text{A.4})$$

Substituting the amplitude into Eq. (2.5), we obtain (for $r \neq 0$):

$$\begin{aligned} V_a(\mathbf{r}) &= \frac{c_1 c_2}{4f_a^2} (\boldsymbol{\sigma}_1 \cdot \nabla) (\boldsymbol{\sigma}_2 \cdot \nabla) \frac{e^{-m_a r}}{4\pi r} \\ &= \frac{c_1 c_2}{4f_a^2} \frac{e^{-m_a r}}{4\pi r^3} [(\boldsymbol{\sigma}_1 \cdot \hat{\mathbf{r}}) (\boldsymbol{\sigma}_2 \cdot \hat{\mathbf{r}}) (3 + 3m_a r + m_a^2 r^2) - (\boldsymbol{\sigma}_1 \cdot \boldsymbol{\sigma}_2) (1 + m_a r)], \end{aligned} \quad (\text{A.5})$$

where $\hat{\mathbf{r}} \equiv \mathbf{r}/r$ is the unit vector. In the axion massless limit, it is reduced to

$$V_a(\mathbf{r}) = \frac{c_1 c_2}{4f_a^2} \frac{1}{4\pi r^3} [3(\boldsymbol{\sigma}_1 \cdot \hat{\mathbf{r}}) (\boldsymbol{\sigma}_2 \cdot \hat{\mathbf{r}}) - (\boldsymbol{\sigma}_1 \cdot \boldsymbol{\sigma}_2)], \quad m_a \rightarrow 0. \quad (\text{A.6})$$

The result of the one-axion force in Eq. (A.5) is well known in the literature [11, 12].² In history, Eq. (A.5) was first used to describe the interaction between two nucleons mediated by the exchange of a neutral pseudoscalar meson [111, 112].

Therefore, the one-axion force depends on the spins of the external fermions, which is the result of the pseudoscalar-type contraction in Eq. (A.3). Furthermore, the one-axion force (A.5) vanishes when performing the spin average over the unpolarized macroscopic objects.

²We notice that our result in Eq. (A.5) agrees with that in Ref. [12] but differs from that in Ref. [11] by an overall minus sign.

This is because

$$(\boldsymbol{\sigma}_1 \cdot \nabla)(\boldsymbol{\sigma}_2 \cdot \nabla) = (\xi_1^*)_\alpha (\xi_1)_\beta (\sigma^i)_{\alpha\beta} (\xi_2^*)_x (\xi_2)_y (\sigma^j)_{xy} \partial_i \partial_j = \langle \alpha, x | \sigma^i \otimes \sigma^j | \beta, y \rangle \partial_i \partial_j, \quad (\text{A.7})$$

where α, β and x, y are indices in the two-dimensional spinor space. After taking the spin average, it becomes

$$\langle \alpha, x | \sigma^i \otimes \sigma^j | \beta, y \rangle \partial_i \partial_j \stackrel{\text{spin average}}{=} \text{Tr}(\sigma^i \otimes \sigma^j) \partial_i \partial_j = 0, \quad (\text{A.8})$$

where in the last step we have used the fact that the trace of the tensor product of any two Pauli matrices vanishes.

As a result, the axion *cannot* mediate long-range forces among unpolarized macroscopic objects at the tree level, which is precisely the reason why the usual fifth-force and equivalence-principle test experiments cannot apply constraints on the axion linear coupling via Fig. 12. In order to get a spin-independent axion force, one needs to include at least two axions as the mediator.

B Pseudoscalar basis versus derivative basis

In this appendix, we briefly review axion effective interactions with fermions. In particular, we pay attention to the structure of couplings in two different axion bases.

The axion appears as the angular mode of a complex scalar in the UV models. After the spontaneous $U(1)$ symmetry breaking, its effective coupling to some fermion ψ can be written as:

$$\mathcal{L} = -m_\psi \bar{\psi} e^{ic_\psi \gamma_5 a/f_a} \psi = -m_\psi \bar{\psi}_L \psi_R e^{ic_\psi a/f_a} + \text{h.c.}, \quad (\text{B.1})$$

where $\psi_{L,R} \equiv \frac{1}{2}(1 \mp \gamma_5)\psi$, m_ψ is the mass of ψ , and c_ψ is a dimensionless parameter depending on ψ . The above coupling has a shift symmetry:

$$a \rightarrow a + c_\psi f_a \theta, \quad \psi_L \rightarrow e^{ic_\psi \theta/2} \psi_L, \quad \psi_R \rightarrow e^{-ic_\psi \theta/2} \psi_R, \quad (\text{B.2})$$

with θ an arbitrary constant. The axion-fermion interactions are obtained by series expanding the exponent in Eq. (B.1):

$$\mathcal{L}_{\text{int}}^{\text{P}} = -ic_\psi m_\psi \frac{a}{f_a} \bar{\psi} \gamma_5 \psi + \frac{1}{2} c_\psi^2 m_\psi \frac{a^2}{f_a^2} \bar{\psi} \psi + \mathcal{O}\left(\frac{a^3}{f_a^3}\right) \quad (\text{pseudoscalar basis}). \quad (\text{B.3})$$

This is the structure of couplings in the *pseudoscalar basis*, where the name comes from the leading pseudoscalar coupling $a \bar{\psi} \gamma_5 \psi$ in Eq. (B.3).

Alternatively, one can change to the *derivative basis* by performing a chiral rotation in

Eq. (B.1) to absorb the axion dependence:

$$\psi_L \rightarrow e^{ic_\psi a/(2f_a)} \psi_L, \quad \psi_R \rightarrow e^{-ic_\psi a/(2f_a)} \psi_R, \quad (\text{B.4})$$

which, after rotation, makes (B.1) a pure mass term $m_\psi \bar{\psi} \psi$. The axion-fermion interaction appears from the kinetic term of ψ in the new basis:

$$\mathcal{L}_{\text{int}}^{\text{d}} = \frac{\partial_\mu a}{2f_a} c_\psi \bar{\psi} \gamma^\mu \gamma_5 \psi \quad (\text{derivative basis}), \quad (\text{B.5})$$

where the axion shift invariance $a \rightarrow a + \text{constant}$ is obvious.

The amplitude predicted by Eqs. (B.3) and (B.5) should agree for any given process,³ meaning that the physical observable should not be dependent on the basis that is selected. For the two-axion force that is the subject of this work, one would expect that the interaction in (B.3), which has both linear and quadratic couplings, would provide the same result as (B.5), which only has linear coupling. In the following section, we shall demonstrate that this is indeed the case.

C Compton scattering of axions

The amplitude relevant to the two-axion force can be calculated by the multiplication of two tree-level Compton scatterings [see Eq. (2.8)]

$$\psi(p_{\text{in}}) + a(k_{\text{in}}) \rightarrow \psi(p_{\text{out}}) + a(k_{\text{out}}), \quad (\text{C.1})$$

as shown in Fig. 13. In this section, we calculate the amplitude explicitly in both the pseudoscalar basis and the derivative basis and show that the results agree with each other.

In the pseudoscalar basis (B.3), there are both linear and quadratic couplings, so all three diagrams (t -channel, u -channel, and contact) in Fig. 13 contribute. Their amplitudes read:

$$\mathcal{M}_t^{\text{P}} = \frac{c_\psi^2}{f_a^2} m_\psi^2 \bar{u}(p_{\text{out}}) \frac{\not{k}_{\text{in}}}{k_{\text{in}}^2 + 2k_{\text{in}} \cdot p_{\text{in}}} u(p_{\text{in}}), \quad (\text{C.2})$$

$$\mathcal{M}_u^{\text{P}} = \frac{c_\psi^2}{f_a^2} m_\psi^2 \bar{u}(p_{\text{out}}) \frac{-\not{k}_{\text{out}}}{k_{\text{out}}^2 - 2k_{\text{out}} \cdot p_{\text{in}}} u(p_{\text{in}}), \quad (\text{C.3})$$

$$\mathcal{M}_c^{\text{P}} = -\frac{c_\psi^2}{f_a^2} m_\psi^2 \bar{u}(p_{\text{out}}) u(p_{\text{in}}). \quad (\text{C.4})$$

So the total amplitude in the pseudoscalar basis is given by

$$\mathcal{M}_C^{\text{P}} = \mathcal{M}_t^{\text{P}} + \mathcal{M}_u^{\text{P}} + \mathcal{M}_c^{\text{P}}$$

³There are an infinite number of interacting terms in Eq. (B.3). To compare with the observable predicted by Eq. (B.5), one should expand the interaction in (B.3) up to $\mathcal{O}((a/f_a)^n)$ for a process involving n axions.

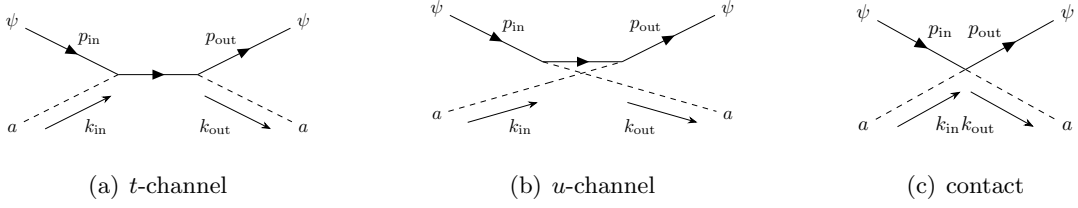


Figure 13. Feynman diagrams for the Compton scattering $\psi(p_{\text{in}}) + a(k_{\text{in}}) \rightarrow \psi(p_{\text{out}}) + a(k_{\text{out}})$ between axions and fermions. Note that under the pseudoscalar basis, all three diagrams are relevant, while under the derivative basis there are only t -channel and u -channel diagrams.

$$= \frac{c_\psi^2}{f_a^2} m_\psi^2 \bar{u}(p_{\text{out}}) \left(\frac{\not{k}_{\text{in}}}{k_{\text{in}}^2 + 2k_{\text{in}} \cdot p_{\text{in}}} - \frac{\not{k}_{\text{out}}}{k_{\text{out}}^2 - 2k_{\text{out}} \cdot p_{\text{in}}} - \frac{1}{m_\psi} \right) u(p_{\text{in}}), \quad (\text{C.5})$$

On the other hand, there is only linear coupling in the derivative basis (B.5), so only the t -channel and u -channel diagrams in Fig. 13 are relevant. Their amplitudes are found to be:

$$\mathcal{M}_t^{\text{d}}(p_{\text{in}}, p_{\text{out}}; k_{\text{in}}, k_{\text{out}}) = \frac{c_\psi^2}{f_a^2} m_\psi^2 \bar{u}(p_{\text{out}}) \left(\frac{\not{k}_{\text{in}}}{k_{\text{in}}^2 + 2k_{\text{in}} \cdot p_{\text{in}}} - \frac{1}{2m_\psi} + \frac{\not{k}_{\text{out}}}{4m_\psi^2} \right) u(p_{\text{in}}), \quad (\text{C.6})$$

$$\mathcal{M}_u^{\text{d}}(p_{\text{in}}, p_{\text{out}}; k_{\text{in}}, k_{\text{out}}) = \frac{c_\psi^2}{f_a^2} m_\psi^2 \bar{u}(p_{\text{out}}) \left(\frac{-\not{k}_{\text{out}}}{k_{\text{out}}^2 - 2k_{\text{out}} \cdot p_{\text{in}}} - \frac{1}{2m_\psi} + \frac{-\not{k}_{\text{in}}}{4m_\psi^2} \right) u(p_{\text{in}}). \quad (\text{C.7})$$

It is obvious that the t -channel and u -channel amplitudes satisfy the crossing symmetry

$$\mathcal{M}_t^{\text{d}}(p_{\text{in}}, p_{\text{out}}; k_{\text{in}}, k_{\text{out}}) = \mathcal{M}_u^{\text{d}}(p_{\text{in}}, p_{\text{out}}; -k_{\text{out}}, -k_{\text{in}}). \quad (\text{C.8})$$

Adding them together, one obtains the total amplitude in the derivative basis:

$$\begin{aligned} \mathcal{M}_C^{\text{d}} &= \mathcal{M}_t^{\text{d}} + \mathcal{M}_u^{\text{d}} \\ &= \frac{c_\psi^2}{f_a^2} m_\psi^2 \bar{u}(p_{\text{out}}) \left(\frac{\not{k}_{\text{in}}}{k_{\text{in}}^2 + 2k_{\text{in}} \cdot p_{\text{in}}} - \frac{\not{k}_{\text{out}}}{k_{\text{out}}^2 - 2k_{\text{out}} \cdot p_{\text{in}}} - \frac{1}{m_\psi} \right) u(p_{\text{in}}), \end{aligned} \quad (\text{C.9})$$

which agrees with the result in the mass basis (C.5). Note that in Eq. (C.9) we have used the momentum conservation $k_{\text{out}} - k_{\text{in}} = p_{\text{in}} - p_{\text{out}}$ and the equation of motion of ψ .

As a result, we have confirmed that, as anticipated, the amplitude of the axion Compton scattering computed in the derivative basis and the pseudoscalar basis agree up to $\mathcal{O}(1/f_a^2)$. Furthermore, since the axion propagators in Eq. (2.8) clearly do not depend on the axion basis, we conclude that the two-axion force and its background correction are also independent of the basis.

D Derivation of V_{bkg} from coherent scattering

In this appendix, we provide an equivalent approach to deriving the background-induced axion force without using the formalism of modified propagator introduced in Sec. 2. The new approach essentially relies on the coherent scattering between background axions and external fermions. A similar derivation with only quadratic couplings (corresponding to the bubble diagram) can be found in [42].

More specifically, our goal is to derive Eq. (2.14) without using the modified propagator in Eq. (2.6). We perform the calculations in the derivative basis, where only the two box diagrams in Fig. 1 are relevant. When in the medium of axions, the background effect contributes in such a way that the background axions are first scattered with ψ_1 (or ψ_2), then the interaction is mediated to ψ_2 (or ψ_1) via an off-shell axion, and finally scattered back to the background, as shown in Fig. 2.

The background effect is determined by the ensemble average of the axion fields. We expand the axion field in the standard way:

$$a(t, \mathbf{x}) = \int \frac{d^3\mathbf{k}}{(2\pi)^3} \frac{1}{\sqrt{2E_{\mathbf{k}}}} \left(a_{\mathbf{k}} e^{-ik \cdot x} + a_{\mathbf{k}}^\dagger e^{ik \cdot x} \right), \quad (\text{D.1})$$

where $E_{\mathbf{k}} \equiv (\mathbf{k}^2 + m_a^2)^{1/2}$, and $a_{\mathbf{k}}$ and $a_{\mathbf{k}}^\dagger$ are the annihilation and creation operators, respectively. Obviously $\langle a(t, \mathbf{x}) \rangle = 0$, where $\langle \dots \rangle$ denotes the ensemble average. However, the mean square (or equivalently, the variance) of the axion field is nonzero

$$\langle a^2(t, \mathbf{x}) \rangle = \int \frac{d^3\mathbf{k}}{(2\pi)^3} \frac{1}{2E_{\mathbf{k}}} f(\mathbf{k}), \quad (\text{D.2})$$

where $f(\mathbf{k})$ is normalized such that $\int d^3\mathbf{k} f(\mathbf{k}) / (2\pi)^3$ is equal to the number density of background axions. To get Eq. (D.2), one needs to use the ensemble average of the number operator:

$$\langle a_{\mathbf{k}}^\dagger a_{\mathbf{k}'} \rangle = (2\pi)^3 f(\mathbf{k}) \delta^{(3)}(\mathbf{k} - \mathbf{k}'). \quad (\text{D.3})$$

As a result, the one-axion effect cannot be affected by the axion background (since $\langle a(t, \mathbf{x}) \rangle = 0$), while the two-axion effect can. For example, the t -channel Compton scattering diagram in Fig. 13(a), when put into the background, becomes

$$\begin{aligned} \langle \mathcal{M}_t \rangle &= - \langle a^2 \rangle \times \frac{c_\psi^2}{4f_a^2} \bar{u}(p_{\text{out}}) \not{k}_{\text{out}} \gamma_5 \frac{1}{\not{p}_{\text{in}} + \not{k}_{\text{in}} - m_\psi} \not{k}_{\text{in}} \gamma_5 u(p_{\text{in}}) \\ &= \int \frac{d^3\mathbf{k}}{(2\pi)^3} \frac{1}{2E_{\mathbf{k}}} f(\mathbf{k}) \mathcal{M}_t, \end{aligned} \quad (\text{D.4})$$

where in the second line we have used Eq. (D.2) and \mathcal{M}_t is given by Eq. (C.6) with the identification $k_{\text{in}} = k$ and $k_{\text{out}} = k + q$.

Then we proceed to calculate the ensemble average of the box diagrams in Fig. 2, each of which can be written as the multiplication of two Compton scatterings. The amplitudes of the first line in Fig. 2 read (from left to right):

$$\langle \mathcal{M}_{tt1} \rangle = \int \frac{d^3\mathbf{k}}{(2\pi)^3} \frac{f(\mathbf{k})}{2E_{\mathbf{k}}} \frac{-1}{(k+q)^2 - m_a^2} \mathcal{M}_t(1) \mathcal{M}_t(2), \quad (\text{D.5})$$

$$\langle \mathcal{M}_{tt2} \rangle = \int \frac{d^3\mathbf{k}}{(2\pi)^3} \frac{f(\mathbf{k} + \mathbf{q})}{2E_{\mathbf{k}+\mathbf{q}}} \frac{-1}{k^2 - m_a^2} \mathcal{M}_t(1) \mathcal{M}_t(2), \quad (\text{D.6})$$

$$\langle \mathcal{M}_{uu1} \rangle = \int \frac{d^3\mathbf{k}}{(2\pi)^3} \frac{f(\mathbf{k})}{2E_{\mathbf{k}}} \frac{-1}{(k+q)^2 - m_a^2} \mathcal{M}_u(1) \mathcal{M}_u(2), \quad (\text{D.7})$$

$$\langle \mathcal{M}_{uu2} \rangle = \int \frac{d^3\mathbf{k}}{(2\pi)^3} \frac{f(\mathbf{k} + \mathbf{q})}{2E_{\mathbf{k}+\mathbf{q}}} \frac{-1}{k^2 - m_a^2} \mathcal{M}_u(1) \mathcal{M}_u(2), \quad (\text{D.8})$$

where Eq. (C.8) is used to transform between \mathcal{M}_t and \mathcal{M}_u , and we have also used the following notations for brevity:

$$\mathcal{M}_j(1) \equiv \mathcal{M}_j(p_1, p'_1, -k, -(k+q)), \quad \mathcal{M}_j(2) \equiv \mathcal{M}_j(p_2, p'_2, k, k+q). \quad (\text{D.9})$$

Therefore, the ensemble average of the amplitude of the ‘‘Box 1’’ diagram in Fig. 1 is given by

$$\begin{aligned} \langle \mathcal{M}_{\text{box},1} \rangle &= \langle \mathcal{M}_{tt1} \rangle + \langle \mathcal{M}_{tt2} \rangle + \langle \mathcal{M}_{uu1} \rangle + \langle \mathcal{M}_{uu2} \rangle \\ &= - \int \frac{d^3\mathbf{k}}{(2\pi)^3} \left[\frac{f(\mathbf{k})}{2E_{\mathbf{k}}} \frac{1}{(k+q)^2 - m_a^2} + \frac{f(\mathbf{k} + \mathbf{q})}{2E_{\mathbf{k}+\mathbf{q}}} \frac{1}{k^2 - m_a^2} \right] [\mathcal{M}_t(1) \mathcal{M}_t(2) + (t \leftrightarrow u)]. \end{aligned} \quad (\text{D.10})$$

Similarly, the amplitudes in the second line of Fig. 2 are given by (from left to right):

$$\langle \mathcal{M}_{tu1} \rangle = \int \frac{d^3\mathbf{k}}{(2\pi)^3} \frac{f(\mathbf{k})}{2E_{\mathbf{k}}} \frac{-1}{(k+q)^2 - m_a^2} \mathcal{M}_t(1) \mathcal{M}_u(2), \quad (\text{D.11})$$

$$\langle \mathcal{M}_{tu2} \rangle = \int \frac{d^3\mathbf{k}}{(2\pi)^3} \frac{f(\mathbf{k} + \mathbf{q})}{2E_{\mathbf{k}+\mathbf{q}}} \frac{-1}{k^2 - m_a^2} \mathcal{M}_t(1) \mathcal{M}_u(2), \quad (\text{D.12})$$

$$\langle \mathcal{M}_{ut1} \rangle = \int \frac{d^3\mathbf{k}}{(2\pi)^3} \frac{f(\mathbf{k})}{2E_{\mathbf{k}}} \frac{-1}{(k+q)^2 - m_a^2} \mathcal{M}_u(1) \mathcal{M}_t(2), \quad (\text{D.13})$$

$$\langle \mathcal{M}_{ut2} \rangle = \int \frac{d^3\mathbf{k}}{(2\pi)^3} \frac{f(\mathbf{k} + \mathbf{q})}{2E_{\mathbf{k}+\mathbf{q}}} \frac{-1}{k^2 - m_a^2} \mathcal{M}_u(1) \mathcal{M}_t(2), \quad (\text{D.14})$$

leading to

$$\langle \mathcal{M}_{\text{box},2} \rangle = \langle \mathcal{M}_{tu1} \rangle + \langle \mathcal{M}_{tu2} \rangle + \langle \mathcal{M}_{ut1} \rangle + \langle \mathcal{M}_{ut2} \rangle$$

$$= - \int \frac{d^3\mathbf{k}}{(2\pi)^3} \left[\frac{f(\mathbf{k})}{2E_{\mathbf{k}}} \frac{1}{(k+q)^2 - m_a^2} + \frac{f(\mathbf{k}+\mathbf{q})}{2E_{\mathbf{k}+\mathbf{q}}} \frac{1}{k^2 - m_a^2} \right] [\mathcal{M}_t(1) \mathcal{M}_u(2) + (t \leftrightarrow u)]. \quad (\text{D.15})$$

The total amplitude is then given by

$$\begin{aligned} \mathcal{M}_{\text{bkg}} &= \langle \mathcal{M}_{\text{box},1} \rangle + \langle \mathcal{M}_{\text{box},2} \rangle \\ &= - \int \frac{d^3\mathbf{k}}{(2\pi)^3} \left[\frac{f(\mathbf{k})}{2E_{\mathbf{k}}} \frac{1}{(k+q)^2 - m_a^2} + \frac{f(\mathbf{k}+\mathbf{q})}{2E_{\mathbf{k}+\mathbf{q}}} \frac{1}{k^2 - m_a^2} \right] \mathcal{M}_C(1) \mathcal{M}_C(2), \end{aligned} \quad (\text{D.16})$$

where $\mathcal{M}_C = \mathcal{M}_t + \mathcal{M}_u$ from Eq. (2.9) is used. Finally, by performing the shift $k \rightarrow k - q$ for the second term in the bracket of Eq. (D.16), we recover the result in Eq. (2.14) as promised. Note that $k^0 = E_{\mathbf{k}}$ is automatically satisfied because background axions are on-shell.

E Relevant integrals

In this appendix, we provide details to calculate the integrals relevant to the background-induced axion force. Using Eq. (2.11), the amplitude in Eq. (2.14) can be recast into a compact form:

$$\mathcal{M}_{\text{bkg}}(q) = - \frac{c_1^2 c_2^2}{f_a^4} m_1^2 m_2^2 \int \frac{d^3\mathbf{k}}{(2\pi)^3} \frac{f(\mathbf{k})}{2E_{\mathbf{k}}} \left[\frac{\mathcal{J}(k)}{(k+q)^2 - m_a^2} + \frac{\mathcal{J}(k-q)}{(k-q)^2 - m_a^2} \right] \Bigg|_{k^0=E_{\mathbf{k}}}, \quad (\text{E.1})$$

where

$$\begin{aligned} \mathcal{J}(k) &= \bar{u}(p'_1) \gamma_\mu u(p_1) \bar{u}(p'_2) \gamma_\nu u(p_2) \left[J_{\text{box},1}^{\mu\nu}(k) + J_{\text{box},2}^{\mu\nu}(k) \right] \\ &\quad + \bar{u}(p'_1) \gamma_\mu u(p_1) \bar{u}(p'_2) u(p_2) J_{\text{tri},1}^\mu(k) + \bar{u}(p'_1) u(p_1) \bar{u}(p'_2) \gamma_\mu u(p_2) J_{\text{tri},2}^\mu(k) \\ &\quad + \bar{u}(p'_1) u(p_1) \bar{u}(p'_2) u(p_2) J_{\text{bub}}(k), \end{aligned} \quad (\text{E.2})$$

and

$$J_{\text{box},1}^{\mu\nu}(k) = \frac{-k^\mu}{k^2 - 2p_1 \cdot k} \frac{k^\nu}{k^2 + 2p_2 \cdot k} + (-k \leftrightarrow k+q), \quad (\text{E.3})$$

$$J_{\text{box},2}^{\mu\nu}(k) = \frac{-k^\mu}{k^2 - 2p_1 \cdot k} \frac{-(k+q)^\nu}{(k+q)^2 - 2p_2 \cdot (k+q)} + (-k \leftrightarrow k+q), \quad (\text{E.4})$$

$$J_{\text{tri},1}^\mu(k) = -\frac{1}{m_2} \frac{-k^\mu}{k^2 - 2p_1 \cdot k} + (-k \leftrightarrow k+q), \quad (\text{E.5})$$

$$J_{\text{tri},2}^\mu(k) = -\frac{1}{m_1} \frac{k^\mu}{k^2 + 2p_2 \cdot k} + (-k \leftrightarrow k+q), \quad (\text{E.6})$$

$$J_{\text{bub}}(k) = \frac{1}{m_1 m_2}. \quad (\text{E.7})$$

Here those J -terms correspond to the contributions from different diagrams in Fig. 1 in the pseudoscalar basis, and each of them corresponds to one term in Eq. (2.15), respectively. Note that terms in Eq. (E.2) that are proportional to \not{q} will vanish after using the equation of motion $\bar{u}(p'_i)\not{q}u(p_i) = 0$.

The background-induced axion force is given by the Fourier transform of the amplitude in the NR limit $q^\mu \approx (0, \mathbf{q})$ [see Eq. (2.5)]:

$$V_{\text{bkg}}(r) = -\frac{c_1^2 c_2^2}{4f_a^4} m_1 m_2 \int \frac{d^3 \mathbf{k}}{(2\pi)^3} \frac{f(\mathbf{k})}{2E_{\mathbf{k}}} \int \frac{d^3 \mathbf{q}}{(2\pi)^3} e^{i\mathbf{q}\cdot\mathbf{r}} \left[\frac{\mathcal{J}_{\text{NR}}(k)}{\mathbf{q}^2 + 2\mathbf{k}\cdot\mathbf{q}} + \frac{\mathcal{J}_{\text{NR}}(k-q)}{\mathbf{q}^2 - 2\mathbf{k}\cdot\mathbf{q}} \right]. \quad (\text{E.8})$$

Expanding the wavefunctions up to the leading order of velocity of external fermions, the \mathcal{J} -factor in Eq. (E.2) becomes

$$\mathcal{J}_{\text{NR}} = 4m_1 m_2 \left[\sum_{i=1}^2 (J_{\text{box},i}^{00} + J_{\text{tri},i}^0) + J_{\text{bub}} \right] + \mathcal{O}(v), \quad (\text{E.9})$$

where $J_{\text{bub}} = 1/(m_1 m_2)$ and in the NR limit, by keeping the leading order of momentum transfer, we have

$$J_{\text{box},1}^{00}(k) = \frac{2E_{\mathbf{k}}^2 (4m_1 m_2 E_{\mathbf{k}}^2 - m_a^4)}{(4m_1^2 E_{\mathbf{k}}^2 - m_a^4) (4m_2^2 E_{\mathbf{k}}^2 - m_a^4)} + \mathcal{O}(\mathbf{q}^2), \quad (\text{E.10})$$

$$J_{\text{box},2}^{00}(k) = \frac{2E_{\mathbf{k}}^2 (4m_1 m_2 E_{\mathbf{k}}^2 + m_a^4)}{(4m_1^2 E_{\mathbf{k}}^2 - m_a^4) (4m_2^2 E_{\mathbf{k}}^2 - m_a^4)} + \mathcal{O}(\mathbf{q}^2), \quad (\text{E.11})$$

$$J_{\text{tri},1}^0(k) = -\frac{4m_1 E_{\mathbf{k}}^2}{m_2 (4m_1^2 E_{\mathbf{k}}^2 - m_a^4)} + \mathcal{O}(\mathbf{q}^2), \quad (\text{E.12})$$

$$J_{\text{tri},2}^0(k) = -\frac{4m_2 E_{\mathbf{k}}^2}{m_1 (4m_2^2 E_{\mathbf{k}}^2 - m_a^4)} + \mathcal{O}(\mathbf{q}^2), \quad (\text{E.13})$$

leading to

$$\begin{aligned} \sum_{i=1}^2 (J_{\text{box},i}^{00} + J_{\text{tri},i}^0) &= \frac{-16E_{\mathbf{k}}^4 m_1 m_2 + 4E_{\mathbf{k}}^2 m_a^4 (m_1/m_2 + m_2/m_1)}{(4m_1^2 E_{\mathbf{k}}^2 - m_a^4) (4m_2^2 E_{\mathbf{k}}^2 - m_a^4)} + \mathcal{O}(\mathbf{q}^2) \\ &= -\frac{1}{m_1 m_2} + \frac{m_a^8}{16m_1^3 m_2^3 E_{\mathbf{k}}^4} + \mathcal{O}(m_a^{12}), \end{aligned} \quad (\text{E.14})$$

where in the second line we have assumed $m_a \ll m_i$ and expanded the result as a series of m_a^2/m_i^2 . Note that the leading term $-1/(m_1 m_2)$ in Eq. (E.14) is exactly cancelled when added to J_{bub} in Eq. (E.7), making the remaining terms all suppressed by the axion mass.

Hence, in the NR limit, we arrive at

$$\mathcal{J}_{\text{NR}}(k) = \mathcal{J}_{\text{NR}}(k-q) = \frac{4m_a^8}{(4m_1^2 E_{\mathbf{k}}^2 - m_a^4) (4m_2^2 E_{\mathbf{k}}^2 - m_a^4)} + \mathcal{O}(\mathbf{q}^2). \quad (\text{E.15})$$

Note that Eq. (E.15) is exact up to $\mathcal{O}(\mathbf{q}^0)$, i.e., we did not assume the hierarchy between m_a and m_i . Substituting Eq. (E.15) back to Eq. (E.8) and neglecting the $\mathcal{O}(\mathbf{q}^2)$ terms, we obtain

$$V_{\text{bkg}}(r) = -\frac{c_1^2 c_2^2}{f_a^4} m_1 m_2 \int \frac{d^3 \mathbf{k}}{(2\pi)^3} \frac{f(\mathbf{k})}{2E_{\mathbf{k}}} \frac{m_a^8}{(4m_1^2 E_{\mathbf{k}}^2 - m_a^4)(4m_2^2 E_{\mathbf{k}}^2 - m_a^4)} \\ \times \int \frac{d^3 \mathbf{q}}{(2\pi)^3} e^{i\mathbf{q}\cdot\mathbf{r}} \left[\frac{1}{\mathbf{q}^2 + 2\mathbf{k}\cdot\mathbf{q}} + \frac{1}{\mathbf{q}^2 - 2\mathbf{k}\cdot\mathbf{q}} \right]. \quad (\text{E.16})$$

The remaining thing is to work out the Fourier transform of \mathbf{q} . To this end, we restore the $i\epsilon$ description (Feynman propagator) to the axion propagators and perform the shift $\mathbf{q} \rightarrow \mathbf{q} - \mathbf{k}$ (or $\mathbf{q} \rightarrow \mathbf{q} + \mathbf{k}$) for the first (or second) term in the bracket:

$$\int \frac{d^3 \mathbf{q}}{(2\pi)^3} e^{i\mathbf{q}\cdot\mathbf{r}} \left[\frac{1}{\mathbf{q}^2 + 2\mathbf{k}\cdot\mathbf{q} - i\epsilon} + \frac{1}{\mathbf{q}^2 - 2\mathbf{k}\cdot\mathbf{q} - i\epsilon} \right] \\ = e^{-i\mathbf{k}\cdot\mathbf{r}} \int \frac{d^3 \mathbf{q}}{(2\pi)^3} e^{i\mathbf{q}\cdot\mathbf{r}} \frac{1}{\mathbf{q}^2 - \mathbf{k}^2 - i\epsilon} + e^{i\mathbf{k}\cdot\mathbf{r}} \int \frac{d^3 \mathbf{q}}{(2\pi)^3} e^{i\mathbf{q}\cdot\mathbf{r}} \frac{1}{\mathbf{q}^2 - \mathbf{k}^2 - i\epsilon} \\ = -\frac{i}{4\pi^2 r} \left[\left(e^{-i\mathbf{k}\cdot\mathbf{r}} + e^{i\mathbf{k}\cdot\mathbf{r}} \right) \int_{-\infty}^{\infty} d|\mathbf{q}| \frac{|\mathbf{q}| e^{i|\mathbf{q}|r}}{|\mathbf{q}|^2 - \mathbf{k}^2 - i\epsilon} \right] \\ = \frac{1}{4\pi r} [\cos(|\mathbf{k}|r - \mathbf{k}\cdot\mathbf{r}) + \cos(|\mathbf{k}|r + \mathbf{k}\cdot\mathbf{r})], \quad (\text{E.17})$$

where in the final step the real part has been implicitly taken.

Substituting Eq. (E.17) into Eq. (E.16), one obtains the final result of the background-induced axion force with the shift-invariant interaction:

$$V_{\text{bkg}}(r) = -\frac{c_1^2 c_2^2}{4\pi r} \frac{m_1 m_2}{f_a^4} \int \frac{d^3 \mathbf{k}}{(2\pi)^3} \frac{f(\mathbf{k})}{2E_{\mathbf{k}}} \frac{m_a^8}{(4m_1^2 E_{\mathbf{k}}^2 - m_a^4)(4m_2^2 E_{\mathbf{k}}^2 - m_a^4)} \\ \times [\cos(|\mathbf{k}|r - \mathbf{k}\cdot\mathbf{r}) + \cos(|\mathbf{k}|r + \mathbf{k}\cdot\mathbf{r})]. \quad (\text{E.18})$$

E.1 Relativistic corrections

In the above calculations, we have taken the NR limit; that is, we neglected all the $\mathcal{O}(\mathbf{q}^2)$ terms in Eq. (E.15). Due to the shift symmetry, cancellation occurs among the $\mathcal{O}(\mathbf{q}^0)$ terms, causing the remaining term to be suppressed by the axion mass.

In the following, we explicitly work out the next-leading-order correction of the \mathcal{J} -factor in Eq. (E.15) under the NR approximation. To simplify the calculation, we introduce

$$P_1 \equiv p_1 + p'_1, \quad P_2 \equiv p_2 + p'_2. \quad (\text{E.19})$$

Recall that the full solution of the Dirac equation in the Pauli-Dirac basis is given by

$$u(p_i) = \sqrt{E_i + m_i} \begin{pmatrix} \xi_i \\ \frac{\boldsymbol{\sigma}\cdot\mathbf{p}_i}{E_i + m_i} \xi_i \end{pmatrix}, \quad i = 1, 2, \quad (\text{E.20})$$

where ξ_i is the two-component spinor of ψ_i . Then the contraction of the wavefunctions gives

$$\bar{u}(p'_i) u(p_i) = \alpha_i \alpha'_i - \frac{\mathbf{P}_i^2 - \mathbf{q}^2 \pm 2\mathbf{q} \cdot (\mathbf{P}_i \times \boldsymbol{\sigma}_i)}{4\alpha_i \alpha'_i}, \quad (\text{E.21})$$

with $\alpha_i \equiv \sqrt{E_i + m_i}$, $\alpha'_i \equiv \sqrt{E'_i + m_i}$ being defined. For signs, ‘+’ corresponds to $i = 1$ while ‘-’ corresponds to $i = 2$. Similarly,

$$\bar{u}(p'_i) \gamma_0 u(p_i) = \alpha_i \alpha'_i + \frac{\mathbf{P}_i^2 - \mathbf{q}^2 \pm 2\mathbf{q} \cdot (\mathbf{P}_i \times \boldsymbol{\sigma}_i)}{4\alpha_i \alpha'_i}, \quad (\text{E.22})$$

$$\bar{u}(p'_i) \gamma_j u(p_i) = -\frac{\alpha_i}{2\alpha'_i} [\mathbf{P}_i \pm \mathbf{q} - (\mathbf{P}_i \pm \mathbf{q}) \times \boldsymbol{\sigma}_i] - \frac{\alpha'_i}{2\alpha_i} [\mathbf{P}_i \mp \mathbf{q} + (\mathbf{P}_i \mp \mathbf{q}) \times \boldsymbol{\sigma}_i]. \quad (\text{E.23})$$

Then we substitute them back to Eq. (E.2) and expand the result as the inverse power of the fermion mass. After some straightforward calculations, one obtains

$$\mathcal{J}(k) = \frac{[(m_a^2 - \mathbf{q} \cdot \mathbf{k})^2 - E_{\mathbf{k}}^2 \mathbf{q}^2]^2}{4m_1^2 m_2^2 E_{\mathbf{k}}^4} + \mathcal{O}\left(\frac{m_a^6}{m_i^6}, \frac{\mathbf{q}^6}{m_i^6}\right), \quad (\text{E.24})$$

$$\mathcal{J}(k - q) = \frac{[(m_a^2 + \mathbf{q} \cdot \mathbf{k})^2 - E_{\mathbf{k}}^2 \mathbf{q}^2]^2}{4m_1^2 m_2^2 E_{\mathbf{k}}^4} + \mathcal{O}\left(\frac{m_a^6}{m_i^6}, \frac{\mathbf{q}^6}{m_i^6}\right). \quad (\text{E.25})$$

As a check, by taking $\mathbf{q}^2 \rightarrow 0$, Eqs. (E.24)-(E.25) are reduced to Eq. (E.15) at the leading order. We are interested in the effect that is not suppressed by the axion mass, so we set $m_a = 0$ for simplicity. Then Eqs. (E.24)-(E.25) are simplified to

$$\mathcal{J}(k) = \mathcal{J}(k - q) = \frac{[(\mathbf{q} \cdot \hat{\mathbf{k}})^2 - \mathbf{q}^2]^2}{4m_1^2 m_2^2} + \mathcal{O}\left(\frac{\mathbf{q}^6}{m_i^6}\right), \quad (\text{E.26})$$

where the hat denotes the unit vector $\hat{\mathbf{k}} \equiv \mathbf{k}/|\mathbf{k}|$. Keeping the leading term and performing the Fourier transform, we get

$$V_{\text{bkg}}(r) = -\frac{c_1^2 c_2^2}{64\pi m_1 m_2 f_a^4} \int \frac{d^3 \mathbf{k}}{(2\pi)^3} \frac{f(\mathbf{k})}{E_{\mathbf{k}}} \left[\nabla^2 - (\hat{\mathbf{k}} \cdot \nabla)^2 \right]^2 \frac{\cos(|\mathbf{k}|r) \cos(\mathbf{k} \cdot \mathbf{r})}{r}. \quad (\text{E.27})$$

Noticing that

$$(\delta_{ij} - \hat{k}_i \hat{k}_j) k_i = (\delta_{ij} - \hat{k}_i \hat{k}_j) k_j = 0, \quad (\text{E.28})$$

one can obtain

$$\begin{aligned}
V_{\text{bkg}}(r) = & -\frac{c_1^2 c_2^2}{64\pi m_1 m_2 f_a^4} \int \frac{d^3 \mathbf{k}}{(2\pi)^3} \frac{f(\mathbf{k})}{E_{\mathbf{k}}} \cos(\mathbf{k} \cdot \mathbf{r}) \\
& \times \left\{ \cos(|\mathbf{k}| r) \left[\frac{9 - 90c^2 + 105c^4}{r^5} + \frac{|\mathbf{k}|^2 (4 - 21c^2 + 45c^4)}{r^3} + \frac{|\mathbf{k}|^4 (1 - 3c^2 + 3c^4)}{r} \right] \right. \\
& \left. + \sin(|\mathbf{k}| r) \left[\frac{|\mathbf{k}| (9 - 90c^2 + 105c^4)}{r^4} - \frac{|\mathbf{k}|^3 (2 + 2c^2 - 18c^4)}{r^2} \right] \right\}, \tag{E.29}
\end{aligned}$$

where $c \equiv \cos(\hat{\mathbf{k}} \cdot \hat{\mathbf{r}})$ has been defined. At long distances, only the $1/r$ component is dominant, so we have

$$V_{\text{bkg}}(r) \approx -\frac{c_1^2 c_2^2}{64\pi r m_1 m_2 f_a^4} \int \frac{d^3 \mathbf{k}}{(2\pi)^3} \frac{f(\mathbf{k})}{E_{\mathbf{k}}} |\mathbf{k}|^4 \cos(\mathbf{k} \cdot \mathbf{r}) \cos(|\mathbf{k}| r) (1 - 3c^2 + 3c^4). \tag{E.30}$$

F Decoherence effects on the axion force

In real fifth-force experiments, both the momentum space and the configuration space have some finite spread, which will suppress the axion force at long distances. In this appendix, we provide calculation details for this decoherence effect.

F.1 Point-like object

We first consider the decoherence effect between two point-like objects. Without loss of generality, we choose \mathbf{v}_a to be aligned with the z -axis and \mathbf{r} in the x - z plane. More specifically, we choose the following coordinates:

$$\mathbf{v}_a = v_a (0, 0, 1), \quad \mathbf{r} = r (s_\alpha, 0, c_\alpha), \quad \mathbf{k} = \kappa (s_\theta c_\varphi, s_\theta s_\varphi, c_\theta), \tag{F.1}$$

where $c_x \equiv \cos x$, $s_x \equiv \sin x$. Then we have

$$\begin{aligned}
\mathbf{k} \cdot \mathbf{r} &= \kappa r (s_\alpha s_\theta c_\varphi + c_\alpha c_\theta), \quad \int d^3 \mathbf{k} = \int_0^\infty d\kappa \kappa^2 \int_0^\pi d\theta s_\theta \int_0^{2\pi} d\varphi, \\
|\mathbf{k} - m_a \mathbf{v}_a|^2 &= \kappa^2 + m_a^2 v_a^2 - 2\kappa m_a v_a c_\theta, \tag{F.2}
\end{aligned}$$

Then the phase-space form factor in Eq. (4.10) can be explicitly written as

$$\begin{aligned}
\mathcal{F}_{\text{PS}}(r, \alpha) &= (2\pi)^{-3/2} \kappa_0^{-3} \int_0^\infty d\kappa \kappa^2 \exp\left(-\frac{\kappa^2 + m_a^2 v_a^2}{2\kappa_0^2}\right) \cos(2\kappa r) \\
&\times \int_0^\pi d\theta s_\theta \exp\left(\frac{\kappa m_a v_a}{\kappa_0^2} c_\theta\right) \int_0^{2\pi} d\varphi \cos[\kappa r (s_\alpha s_\theta c_\varphi + c_\alpha c_\theta)]. \tag{F.3}
\end{aligned}$$

Integrating out φ and using $m_a v_a = \sqrt{2}\kappa_0$, one obtains

$$\mathcal{F}_{\text{PS}}(r, \alpha) = \frac{e^{-1}}{\sqrt{2\pi}\kappa_0^3} \int_0^\infty d\kappa \kappa^2 \cos(\kappa r) e^{-\frac{\kappa^2}{2\kappa_0^2}} \int_{-1}^1 dz e^{\frac{\sqrt{2}\kappa z}{\kappa_0}} \cos(\kappa r c_\alpha z) J_0\left(\kappa r s_\alpha \sqrt{1-z^2}\right), \quad (\text{F.4})$$

where $z \equiv c_\theta$ and J_0 is the Bessel function of the first kind. For the special case of $\alpha = 0$, i.e., when the DM wind is parallel to \mathbf{r} , we can work out the integral analytically:

$$\begin{aligned} \mathcal{F}_{\text{PS}}(r, 0) &= \frac{2e^{-1}}{\sqrt{2\pi}\kappa_0^2(2+\kappa_0^2 r^2)} \int_0^\infty d\kappa \kappa \cos(\kappa r) e^{-\frac{\kappa^2}{2\kappa_0^2}} \\ &\quad \times \left[\kappa_0 r \cosh\left(\frac{\sqrt{2}\kappa}{\kappa_0}\right) \sin(\kappa r) + \sqrt{2} \sinh\left(\frac{\sqrt{2}\kappa}{\kappa_0}\right) \cos(\kappa r) \right] \\ &= \frac{1}{2+\kappa_0^2 r^2} \left\{ 1 + e^{-2\kappa_0^2 r^2} \left[(1+\kappa_0^2 r^2) \cos(2\sqrt{2}\kappa_0 r) - \frac{\kappa_0 r}{\sqrt{2}} \sin(2\sqrt{2}\kappa_0 r) \right] \right\}. \quad (\text{F.5}) \end{aligned}$$

It is easy to check that $\mathcal{F}_{\text{PS}} \rightarrow 1$ for $\kappa_0 r \ll 1$ and $\mathcal{F}_{\text{PS}} \rightarrow 1/(\kappa_0^2 r^2)$ for $\kappa_0 r \gg 1$.

F.2 Finite-size object

It is straightforward to generalize Eq. (F.3) to arbitrary finite-size objects by integrating over the configuration space. In the following, we take the geometric setup in Fig. 5 as an example, where the source is a ball with a radius R and the target is approximated to be point-like.

We choose the center of the ball O as the reference point, and the vector from O to the target is denoted by \mathbf{r} . The angle between \mathbf{r} and the preferred direction of the axion DM wind is α . For an arbitrary point located at \mathbf{r}' in the ball, its contribution to V_{bkg} is known, and the form factor is described by Eq. (F.3) with the replacement $r \rightarrow |\mathbf{r} - \mathbf{r}'|$ and $\alpha \rightarrow \alpha_{\text{eff}}$, where α_{eff} denotes the angle between $\mathbf{r} - \mathbf{r}'$ and \mathbf{v}_a . The total form factor, including both phase-space and finite-size decoherence effects, is obtained by integrating \mathcal{F}_{PS} over the ball [see Eq. (4.17)]:

$$\mathcal{F}_{\text{tot}}(r, \alpha) = \frac{3r}{4\pi R^3} \int_{\text{ball}} d^3\mathbf{r}' \frac{\mathcal{F}_{\text{PS}}(|\mathbf{r} - \mathbf{r}'|, \alpha_{\text{eff}})}{|\mathbf{r} - \mathbf{r}'|}. \quad (\text{F.6})$$

We choose the coordinate of \mathbf{r}' such that

$$\mathbf{r}' = r'(s_\beta c_\gamma, s_\beta s_\gamma, c_\beta), \quad \int_{\text{ball}} d^3\mathbf{r}' = \int_0^R dr' r'^2 \int_0^\pi d\beta s_\beta \int_0^{2\pi} d\gamma. \quad (\text{F.7})$$

Combining Eqs. (F.7) and (F.1) and using the geometric relation, one obtains

$$\mathcal{F}_{\text{tot}}(r, \alpha) = \frac{3r}{4\pi R^3} \int_0^R dr' r'^2 \int_0^\pi d\beta s_\beta \int_0^{2\pi} d\gamma \frac{\mathcal{F}_{\text{PS}}(|\mathbf{r} - \mathbf{r}'|, \alpha_{\text{eff}})}{|\mathbf{r} - \mathbf{r}'|}, \quad (\text{F.8})$$

where

$$|\mathbf{r} - \mathbf{r}'| = \sqrt{r^2 + r'^2 - 2rr'(s_\alpha s_\beta c_\gamma + c_\alpha c_\beta)}, \quad \alpha_{\text{eff}} = \arccos\left(\frac{rc_\alpha - r'c_\beta}{|\mathbf{r} - \mathbf{r}'|}\right). \quad (\text{F.9})$$

G Axion forces from solar axion flux

In this appendix, we calculate the axion force induced by solar axion flux. The general formula of V_{bkg} for a directional axion beam is given in Eqs. (3.15)-(3.16), while the energy spectrum of the solar axion flux is described by Eq. (4.18).

The integrals in Eqs. (3.15)-(3.16) can be analytically worked out using the following identity:

$$\int_0^\infty d\kappa \kappa^b e^{-c\kappa} \cos(d\kappa) = (c^2 + d^2)^{-\frac{b+1}{2}} \cos\left[(b+1) \arctan\left(\frac{d}{c}\right)\right] \Gamma(b+1), \quad (\text{G.1})$$

where b, c, d are arbitrary positive constants.

Comparing the axion force with gravity, we obtain

$$\frac{V_{\text{solar}}^{\text{shift}}}{V_{\text{grav}}} \approx 10^{-15} \left(\frac{\mu}{\mu_{\text{QCD}}}\right)^2 \left(\frac{2.5 \times 10^3 \text{ GeV}}{f_a}\right)^4 \mathcal{D}_1(\alpha), \quad (\text{G.2})$$

$$\frac{V_{\text{solar}}^{\text{rel}}}{V_{\text{grav}}} \approx 10^{-15} \left(\frac{48 \text{ MeV}}{f_a/c_N}\right)^4 (1 - 3 \cos^2 \alpha + 3 \cos^4 \alpha) \mathcal{D}_2(\alpha), \quad (\text{G.3})$$

where the decoherence factors are given by:

$$\begin{aligned} \mathcal{D}_1(\alpha) \approx & \left(1 + 1.5 r_{\text{\AA}}^2 \sin^4 \frac{\alpha}{2}\right)^{-1.2} \cos\left[2.5 \arctan\left(1.2 r_{\text{\AA}} \sin^2 \frac{\alpha}{2}\right)\right] \\ & + \left(1 + 1.5 r_{\text{\AA}}^2 \cos^4 \frac{\alpha}{2}\right)^{-1.2} \cos\left[2.5 \arctan\left(1.2 r_{\text{\AA}} \cos^2 \frac{\alpha}{2}\right)\right], \end{aligned} \quad (\text{G.4})$$

$$\begin{aligned} \mathcal{D}_2(\alpha) \approx & \left(1 + 1.5 r_{\text{\AA}}^2 \sin^4 \frac{\alpha}{2}\right)^{-3.2} \cos\left[6.5 \arctan\left(1.2 r_{\text{\AA}} \sin^2 \frac{\alpha}{2}\right)\right] \\ & + \left(1 + 1.5 r_{\text{\AA}}^2 \cos^4 \frac{\alpha}{2}\right)^{-3.2} \cos\left[6.5 \arctan\left(1.2 r_{\text{\AA}} \cos^2 \frac{\alpha}{2}\right)\right], \end{aligned} \quad (\text{G.5})$$

with

$$r_{\text{\AA}} \equiv \frac{r}{0.1 \text{ nm}}. \quad (\text{G.6})$$

Note that the typical energy scale of solar axion flux is $\kappa_0 \sim \text{keV}$, with the de Broglie wavelength $\lambda_{\text{dB}} \sim 1/\kappa_0 \sim 0.2 \text{ nm}$. So, for $r \gg 0.1 \text{ nm}$, the decoherence effect will suppress the sensitivity. This can be seen from Eqs. (G.4)-(G.5). For $r_{\text{\AA}} \alpha^2 \gg 1$, \mathcal{D}_1 and \mathcal{D}_2 are suppressed by the inverse power of $r_{\text{\AA}}$:

$$\mathcal{D}_1(\alpha \gg 1/\sqrt{r_{\text{\AA}}}) \approx -0.43 \times r_{\text{\AA}}^{-2.4} \left[\left(\sin \frac{\alpha}{2}\right)^{-4.8} + \left(\cos \frac{\alpha}{2}\right)^{-4.8} \right], \quad (\text{G.7})$$

$$\mathcal{D}_2 (\alpha \gg 1/\sqrt{r_{\text{A}}}) \approx -0.19 \times r_{\text{A}}^{-6.4} \left[\left(\sin \frac{\alpha}{2} \right)^{-12.8} + \left(\cos \frac{\alpha}{2} \right)^{-12.8} \right]. \quad (\text{G.8})$$

On the other hand, in the small angle limit, $\alpha \ll 1/\sqrt{r_{\text{A}}}$, we have $\mathcal{D}_1, \mathcal{D}_2 \sim \mathcal{O}(1)$.

References

- [1] F. Wilczek, *Problem of Strong P and T Invariance in the Presence of Instantons*, *Phys. Rev. Lett.* **40** (1978) 279–282.
- [2] S. Weinberg, *A New Light Boson?*, *Phys. Rev. Lett.* **40** (1978) 223–226.
- [3] R. D. Peccei and H. R. Quinn, *Constraints Imposed by CP Conservation in the Presence of Instantons*, *Phys. Rev. D* **16** (1977) 1791–1797.
- [4] R. D. Peccei and H. R. Quinn, *CP Conservation in the Presence of Instantons*, *Phys. Rev. Lett.* **38** (1977) 1440–1443.
- [5] M. Dine and W. Fischler, *The Not So Harmless Axion*, *Phys. Lett. B* **120** (1983) 137–141.
- [6] J. Preskill, M. B. Wise, and F. Wilczek, *Cosmology of the Invisible Axion*, *Phys. Lett. B* **120** (1983) 127–132.
- [7] A. Arvanitaki, S. Dimopoulos, S. Dubovsky, N. Kaloper, and J. March-Russell, *String Axiverse*, *Phys. Rev. D* **81** (2010) 123530, [[0905.4720](#)].
- [8] P. Arias, D. Cadamuro, M. Goodsell, J. Jaeckel, J. Redondo, and A. Ringwald, *WISPy Cold Dark Matter*, *JCAP* **06** (2012) 013, [[1201.5902](#)].
- [9] D. J. E. Marsh, *Axion Cosmology*, *Phys. Rept.* **643** (2016) 1–79, [[1510.07633](#)].
- [10] L. Di Luzio, M. Giannotti, E. Nardi, and L. Visinelli, *The landscape of QCD axion models*, *Phys. Rept.* **870** (2020) 1–117, [[2003.01100](#)].
- [11] J. E. Moody and F. Wilczek, *NEW MACROSCOPIC FORCES?*, *Phys. Rev. D* **30** (1984) 130.
- [12] R. Daido and F. Takahashi, *The sign of the dipole–dipole potential by axion exchange*, *Phys. Lett. B* **772** (2017) 127–129, [[1704.00155](#)].
- [13] H. Georgi and L. Randall, *Flavor Conserving CP Violation in Invisible Axion Models*, *Nucl. Phys. B* **276** (1986) 241–252.
- [14] Y. V. Stadnik and V. V. Flambaum, *Axion-induced effects in atoms, molecules, and nuclei: Parity nonconservation, anapole moments, electric dipole moments, and spin-gravity and spin-axion momentum couplings*, *Phys. Rev. D* **89** (2014), no. 4 043522, [[1312.6667](#)].
- [15] A. Arvanitaki and A. A. Geraci, *Resonantly Detecting Axion-Mediated Forces with Nuclear Magnetic Resonance*, *Phys. Rev. Lett.* **113** (2014), no. 16 161801, [[1403.1290](#)].
- [16] **ARIADNE Collaboration**, A. A. Geraci *et al.*, *Progress on the ARIADNE axion experiment*, *Springer Proc. Phys.* **211** (2018) 151–161, [[1710.05413](#)].
- [17] C. A. J. O’Hare and E. Vitagliano, *Cornering the axion with CP-violating interactions*, *Phys. Rev. D* **102** (2020), no. 11 115026, [[2010.03889](#)].
- [18] S. Okawa, M. Pospelov, and A. Ritz, *Long-range axion forces and hadronic CP violation*, *Phys. Rev. D* **105** (2022), no. 7 075003, [[2111.08040](#)].

- [19] A. Arvanitaki, J. Engel, A. A. Geraci, A. Madden, A. Hepburn, and K. Van Tilburg, *The Ferroaxionic Force*, [2411.10516](#).
- [20] A. Hees, O. Minazzoli, E. Savalle, Y. V. Stadnik, and P. Wolf, *Violation of the equivalence principle from light scalar dark matter*, *Phys. Rev. D* **98** (2018), no. 6 064051, [[1807.04512](#)].
- [21] X. Gan and D. Liu, *Cosmologically varying kinetic mixing*, *JHEP* **11** (2023) 031, [[2302.03056](#)].
- [22] G. Vasilakis, J. M. Brown, T. W. Kornack, and M. V. Romalis, *Limits on new long range nuclear spin-dependent forces set with a $K - He-3$ co-magnetometer*, *Phys. Rev. Lett.* **103** (2009) 261801, [[0809.4700](#)].
- [23] L. Hunter, J. Gordon, S. Peck, D. Ang, and J. F. Lin, *Using the Earth as a Polarized Electron Source to Search for Long-Range Spin-Spin Interactions*, *Science* **339** (2013), no. 6122 928–932.
- [24] B. R. Heckel, W. A. Terrano, and E. G. Adelberger, *Limits on Exotic Long-Range Spin-Spin Interactions of Electrons*, *Phys. Rev. Lett.* **111** (2013), no. 15 151802.
- [25] S. Kotler, R. Ozeri, and D. F. J. Kimball, *Constraints on exotic dipole-dipole couplings between electrons at the micrometer scale*, *Phys. Rev. Lett.* **115** (2015), no. 8 081801, [[1501.07891](#)].
- [26] W. A. Terrano, E. G. Adelberger, J. G. Lee, and B. R. Heckel, *Short-range spin-dependent interactions of electrons: a probe for exotic pseudo-Goldstone bosons*, *Phys. Rev. Lett.* **115** (2015), no. 20 201801, [[1508.02463](#)].
- [27] J. A. Grifols and S. Tortosa, *Residual long range pseudoscalar forces between unpolarized macroscopic bodies*, *Phys. Lett. B* **328** (1994) 98–102, [[hep-ph/9404249](#)].
- [28] F. Ferrer and J. A. Grifols, *Long range forces from pseudoscalar exchange*, *Phys. Rev. D* **58** (1998) 096006, [[hep-ph/9805477](#)].
- [29] E. Fischbach and D. E. Krause, *New limits on the couplings of light pseudoscalars from equivalence principle experiments*, *Phys. Rev. Lett.* **82** (1999) 4753–4756, [[hep-ph/9905408](#)].
- [30] M. Bauer and G. Rostagni, *Fifth Forces from QCD Axions Scale Differently*, *Phys. Rev. Lett.* **132** (2024), no. 10 101802, [[2307.09516](#)].
- [31] G. Rostagni, *Effective Operators and Long-Range Forces for Dark Matter*. PhD thesis, Durham U., 2024.
- [32] M. Ghosh, Y. Grossman, W. Tangarife, X.-J. Xu, and B. Yu, *Neutrino forces in neutrino backgrounds*, *JHEP* **02** (2023) 092, [[2209.07082](#)].
- [33] M. Ghosh, Y. Grossman, W. Tangarife, X.-J. Xu, and B. Yu, *The neutrino force in neutrino backgrounds: Spin dependence and parity-violating effects*, *JHEP* **07** (2024) 107, [[2405.16801](#)].
- [34] D. Blas, I. Esteban, M. C. Gonzalez-Garcia, and J. Salvado, *On neutrino-mediated potentials in a neutrino background*, *JHEP* **04** (2023) 039, [[2212.03889](#)].
- [35] H. Fukuda and S. Shirai, *Detection of QCD axion dark matter by coherent scattering*, *Phys. Rev. D* **105** (2022), no. 9 095030, [[2112.13536](#)].
- [36] H. Kim and G. Perez, *Oscillations of atomic energy levels induced by QCD axion dark matter*, *Phys. Rev. D* **109** (2024), no. 1 015005, [[2205.12988](#)].

- [37] A. Banerjee, G. Perez, M. Safronova, I. Savoray, and A. Shalit, *The phenomenology of quadratically coupled ultra light dark matter*, *JHEP* **10** (2023) 042, [[2211.05174](#)].
- [38] T. Bouley, P. Sørensen, and T.-T. Yu, *Constraints on ultralight scalar dark matter with quadratic couplings*, *JHEP* **03** (2023) 104, [[2211.09826](#)].
- [39] C. Beadle, S. A. R. Ellis, J. Quevillon, and P. N. Hoa Vuong, *Quadratic coupling of the axion to photons*, *Phys. Rev. D* **110** (2024), no. 3 035019, [[2307.10362](#)].
- [40] H. Kim, A. Lenoci, G. Perez, and W. Ratzinger, *Probing an ultralight QCD axion with electromagnetic quadratic interaction*, *Phys. Rev. D* **109** (2024), no. 1 015030, [[2307.14962](#)].
- [41] H. Day, D. Liu, M. A. Luty, and Y. Zhao, *Blowing in the dark matter wind*, *JHEP* **07** (2024) 136, [[2312.13345](#)].
- [42] K. Van Tilburg, *Wake forces in a background of quadratically coupled mediators*, *Phys. Rev. D* **109** (2024), no. 9 096036, [[2401.08745](#)].
- [43] S. Barbosa and S. Fichet, *Background-induced forces from dark relics*, *JHEP* **01** (2025) 021, [[2403.13894](#)].
- [44] M. Bauer and S. Chakraborti, *On the Validity of Bounds on Light Axions for $f \lesssim 10^{15}$ GeV*, [2408.06408](#).
- [45] M. Bauer, S. Chakraborti, and G. Rostagni, *Axion Bounds from Quantum Technology*, [2408.06412](#).
- [46] S.-P. Li and K.-P. Xie, *Photon proliferation from N-body dark matter annihilation*, [2412.15749](#).
- [47] K. Zhou, *Ponderomotive Effects of Ultralight Dark Matter*, [2502.01725](#).
- [48] A. Banerjee, I. M. Bloch, Q. Bonnefoy, S. A. R. Ellis, G. Perez, I. Savoray, K. Springmann, and Y. V. Stadnik, *Momentum and Matter Matter for Axion Dark Matter Matters on Earth*, [2502.04455](#).
- [49] Y. G. del Castillo, B. Hammett, and J. Jaeckel, *Enhanced Axion-wind near Earth’s Surface*, [2502.04456](#).
- [50] X. Gan, D. Liu, D. Liu, X. Luo, and B. Yu, *Detecting Ultralight Dark Matter with Matter Effect, to appear soon*.
- [51] C. J. Horowitz and J. T. Pantaleone, *Long range forces from the cosmological neutrinos background*, *Phys. Lett. B* **319** (1993) 186–190, [[hep-ph/9306222](#)].
- [52] F. Ferrer, J. A. Grifols, and M. Nowakowski, *Long range forces induced by neutrinos at finite temperature*, *Phys. Lett. B* **446** (1999) 111–116, [[hep-ph/9806438](#)].
- [53] F. Ferrer, J. A. Grifols, and M. Nowakowski, *Long range neutrino forces in the cosmic relic neutrino background*, *Phys. Rev. D* **61** (2000) 057304, [[hep-ph/9906463](#)].
- [54] F. Ferrer and M. Nowakowski, *Higgs and Goldstone bosons mediated long range forces*, *Phys. Rev. D* **59** (1999) 075009, [[hep-ph/9810550](#)].
- [55] F. Ferrer and J. A. Grifols, *Effects of Bose-Einstein condensation on forces among bodies sitting in a boson heat bath*, *Phys. Rev. D* **63** (2001) 025020, [[hep-ph/0001185](#)].

- [56] J. A. Dror, H. Murayama, and N. L. Rodd, *Cosmic axion background*, *Phys. Rev. D* **103** (2021), no. 11 115004, [[2101.09287](#)]. [Erratum: *Phys.Rev.D* 106, 119902 (2022)].
- [57] **CAST Collaboration**, S. Andriamonje *et al.*, *An Improved limit on the axion-photon coupling from the CAST experiment*, *JCAP* **04** (2007) 010, [[hep-ex/0702006](#)].
- [58] D. Nötzold and G. Raffelt, *Neutrino dispersion at finite temperature and density*, *Nucl. Phys. B* **307** (1988) 924–936.
- [59] K. Freese, J. A. Frieman, and A. Gould, *Signal Modulation in Cold Dark Matter Detection*, *Phys. Rev. D* **37** (1988) 3388–3405.
- [60] M. Hoeft, J. P. Mucket, and S. Gottlober, *Velocity dispersion profile in dark matter halos*, *Astrophys. J.* **602** (2004) 162–169, [[astro-ph/0311083](#)].
- [61] A. Faltenbacher and J. Diemand, *Velocity distributions in clusters of galaxies*, *Mon. Not. Roy. Astron. Soc.* **369** (2006) 1698–1702, [[astro-ph/0602197](#)].
- [62] M. Vogelsberger, A. Helmi, V. Springel, S. D. M. White, J. Wang, C. S. Frenk, A. Jenkins, A. D. Ludlow, and J. F. Navarro, *Phase-space structure in the local dark matter distribution and its signature in direct detection experiments*, *Mon. Not. Roy. Astron. Soc.* **395** (2009) 797–811, [[0812.0362](#)].
- [63] **Planck Collaboration**, N. Aghanim *et al.*, *Planck 2018 results. VI. Cosmological parameters*, *Astron. Astrophys.* **641** (2020) A6, [[1807.06209](#)]. [Erratum: *Astron.Astrophys.* 652, C4 (2021)].
- [64] **MICROSCOPE Collaboration**, P. Touboul *et al.*, *MICROSCOPE Mission: Final Results of the Test of the Equivalence Principle*, *Phys. Rev. Lett.* **129** (2022), no. 12 121102, [[2209.15487](#)].
- [65] S. Schlamminger, K. Y. Choi, T. A. Wagner, J. H. Gundlach, and E. G. Adelberger, *Test of the equivalence principle using a rotating torsion balance*, *Phys. Rev. Lett.* **100** (2008) 041101, [[0712.0607](#)].
- [66] G. L. Smith, C. D. Hoyle, J. H. Gundlach, E. G. Adelberger, B. R. Heckel, and H. E. Swanson, *Short range tests of the equivalence principle*, *Phys. Rev. D* **61** (2000) 022001, [[2405.10982](#)].
- [67] J. K. Hoskins, R. D. Newman, R. Spero, and J. Schultz, *Experimental tests of the gravitational inverse square law for mass separations from 2-cm to 105-cm*, *Phys. Rev. D* **32** (1985) 3084–3095.
- [68] S.-Q. Yang, B.-F. Zhan, Q.-L. Wang, C.-G. Shao, L.-C. Tu, W.-H. Tan, and J. Luo, *Test of the Gravitational Inverse Square Law at Millimeter Ranges*, *Phys. Rev. Lett.* **108** (2012) 081101.
- [69] D. J. Kapner, T. S. Cook, E. G. Adelberger, J. H. Gundlach, B. R. Heckel, C. D. Hoyle, and H. E. Swanson, *Tests of the gravitational inverse-square law below the dark-energy length scale*, *Phys. Rev. Lett.* **98** (2007) 021101, [[hep-ph/0611184](#)].
- [70] W.-H. Tan *et al.*, *Improvement for Testing the Gravitational Inverse-Square Law at the Submillimeter Range*, *Phys. Rev. Lett.* **124** (2020), no. 5 051301.
- [71] J. G. Lee, E. G. Adelberger, T. S. Cook, S. M. Fleischer, and B. R. Heckel, *New Test of the Gravitational $1/r^2$ Law at Separations down to 52 μm* , *Phys. Rev. Lett.* **124** (2020), no. 10 101101, [[2002.11761](#)].

- [72] D. C. Moore and A. A. Geraci, *Searching for new physics using optically levitated sensors*, *Quantum Sci. Technol.* **6** (2021) 014008, [[2008.13197](#)].
- [73] Y. J. Chen, W. K. Tham, D. E. Krause, D. Lopez, E. Fischbach, and R. S. Decca, *Stronger Limits on Hypothetical Yukawa Interactions in the 30–8000 nm Range*, *Phys. Rev. Lett.* **116** (2016), no. 22 221102, [[1410.7267](#)].
- [74] E. G. Adelberger, J. H. Gundlach, B. R. Heckel, S. Hoedl, and S. Schlamminger, *Torsion balance experiments: A low-energy frontier of particle physics*, *Prog. Part. Nucl. Phys.* **62** (2009) 102–134.
- [75] T. A. Wagner, S. Schlamminger, J. H. Gundlach, and E. G. Adelberger, *Torsion-balance tests of the weak equivalence principle*, *Class. Quant. Grav.* **29** (2012) 184002, [[1207.2442](#)].
- [76] A. Franklin and E. Fischbach, *The rise and fall of the fifth force: Discovery, pursuit, and justification in modern physics*. Springer, 2016.
- [77] G. Grilli di Cortona, E. Hardy, J. Pardo Vega, and G. Villadoro, *The QCD axion, precisely*, *JHEP* **01** (2016) 034, [[1511.02867](#)].
- [78] B. Holdom and M. E. Peskin, *Raising the Axion Mass*, *Nucl. Phys. B* **208** (1982) 397–412.
- [79] V. A. Rubakov, *Grand unification and heavy axion*, *JETP Lett.* **65** (1997) 621–624, [[hep-ph/9703409](#)].
- [80] H. Fukuda, K. Harigaya, M. Ibe, and T. T. Yanagida, *Model of visible QCD axion*, *Phys. Rev. D* **92** (2015), no. 1 015021, [[1504.06084](#)].
- [81] S. Dimopoulos, A. Hook, J. Huang, and G. Marques-Tavares, *A collider observable QCD axion*, *JHEP* **11** (2016) 052, [[1606.03097](#)].
- [82] T. Gherghetta, N. Nagata, and M. Shifman, *A Visible QCD Axion from an Enlarged Color Group*, *Phys. Rev. D* **93** (2016), no. 11 115010, [[1604.01127](#)].
- [83] P. Agrawal and K. Howe, *Factoring the Strong CP Problem*, *JHEP* **12** (2018) 029, [[1710.04213](#)].
- [84] A. Hook, S. Kumar, Z. Liu, and R. Sundrum, *High Quality QCD Axion and the LHC*, *Phys. Rev. Lett.* **124** (2020), no. 22 221801, [[1911.12364](#)].
- [85] T. Gherghetta, V. V. Khoze, A. Pomarol, and Y. Shirman, *The Axion Mass from 5D Small Instantons*, *JHEP* **03** (2020) 063, [[2001.05610](#)].
- [86] K. J. Kelly, S. Kumar, and Z. Liu, *Heavy axion opportunities at the DUNE near detector*, *Phys. Rev. D* **103** (2021), no. 9 095002, [[2011.05995](#)].
- [87] D. I. Dunsky, L. J. Hall, and K. Harigaya, *A heavy QCD axion and the mirror world*, *JHEP* **02** (2024) 212, [[2302.04274](#)].
- [88] **Particle Data Group Collaboration**, S. Navas *et al.*, *Review of particle physics*, *Phys. Rev. D* **110** (2024), no. 3 030001.
- [89] G. Raffelt and D. Seckel, *Bounds on Exotic Particle Interactions from SN 1987a*, *Phys. Rev. Lett.* **60** (1988) 1793.
- [90] M. S. Turner, *Axions from SN 1987a*, *Phys. Rev. Lett.* **60** (1988) 1797.

- [91] A. Burrows, M. S. Turner, and R. P. Brinkmann, *Axions and SN 1987a*, *Phys. Rev. D* **39** (1989) 1020.
- [92] G. G. Raffelt, *Astrophysical methods to constrain axions and other novel particle phenomena*, *Phys. Rept.* **198** (1990) 1–113.
- [93] H. Primakoff, *Photo-production of neutral mesons in nuclear electric fields and the mean life of the neutral meson*, *Phys. Rev.* **81** (Mar, 1951) 899–899.
- [94] K. van Bibber, P. M. McIntyre, D. E. Morris, and G. G. Raffelt, *A Practical Laboratory Detector for Solar Axions*, *Phys. Rev. D* **39** (1989) 2089.
- [95] Q.-f. Wu and X.-J. Xu, *A comprehensive calculation of the Primakoff process and the solar axion flux*, *JCAP* **07** (2024) 013, [[2402.16083](#)].
- [96] M. S. Safronova, D. Budker, D. DeMille, D. F. J. Kimball, A. Derevianko, and C. W. Clark, *Search for New Physics with Atoms and Molecules*, *Rev. Mod. Phys.* **90** (2018), no. 2 025008, [[1710.01833](#)].
- [97] I. Klaft *et al.*, *Precision Laser Spectroscopy of the Ground State Hyperfine Splitting of Hydrogenlike Bi-82 + 209*, *Phys. Rev. Lett.* **73** (1994) 2425–2427.
- [98] W. Liu *et al.*, *High precision measurements of the ground state hyperfine structure interval of muonium and of the muon magnetic moment*, *Phys. Rev. Lett.* **82** (1999) 711–714.
- [99] J. Ullmann, Z. Andelkovic, C. Brandau, A. Dax, W. Geithner, C. Geppert, C. Gorges, M. Hammen, V. Hannen, S. Kaufmann, *et al.*, *High precision hyperfine measurements in bismuth challenge bound-state strong-field qed*, *Nature communications* **8** (2017), no. 1 15484.
- [100] C. S. Wood, S. C. Bennett, D. Cho, B. P. Masterson, J. L. Roberts, C. E. Tanner, and C. E. Wieman, *Measurement of parity nonconservation and an anapole moment in cesium*, *Science* **275** (1997) 1759–1763.
- [101] M. A. Bouchiat and C. Bouchiat, *Parity violation in atoms*, *Rept. Prog. Phys.* **60** (1997) 1351–1396.
- [102] C. Wieman and A. Derevianko, *Atomic parity violation and the standard model*, [1904.00281](#).
- [103] V. A. Dzuba, V. V. Flambaum, P. Munro-Laylim, and Y. V. Stadnik, *Probing Long-Range Neutrino-Mediated Forces with Atomic and Nuclear Spectroscopy*, *Phys. Rev. Lett.* **120** (2018), no. 22 223202, [[1711.03700](#)]. [Erratum: *Phys.Rev.Lett.* 129, 239901 (2022)].
- [104] M. Ghosh, Y. Grossman, and W. Tangarife, *Probing the two-neutrino exchange force using atomic parity violation*, *Phys. Rev. D* **101** (2020), no. 11 116006, [[1912.09444](#)].
- [105] P. Munro-Laylim, V. A. Dzuba, and V. V. Flambaum, *Effects of the long-range neutrino-mediated force in atomic phenomena*, [2207.07325](#).
- [106] M. Ghosh, Y. Grossman, C. Sieng, and B. Yu, *The neutrino force at all length scales*, [2410.19059](#).
- [107] J. C. Berengut *et al.*, *Probing New Long-Range Interactions by Isotope Shift Spectroscopy*, *Phys. Rev. Lett.* **120** (2018) 091801, [[1704.05068](#)].
- [108] C. G. Parthey, A. Matveev, J. Alnis, R. Pohl, T. Udem, U. D. Jentschura, N. Kolachevsky, and T. W. Hänsch, *Precision Measurement of the Hydrogen-Deuterium 1S-2S Isotope Shift*, *Phys. Rev. Lett.* **104** (2010) 233001.

- [109] V. Meyer *et al.*, *Measurement of the 1s - 2s energy interval in muonium*, *Phys. Rev. Lett.* **84** (2000) 1136, [[hep-ex/9907013](#)].
- [110] P. Crivelli, *The Mu-MASS (Muonium LASer SpectroScopy) experiment*, *Hyperfine Interact.* **239** (2018), no. 1 49, [[1811.00310](#)].
- [111] K. A. Brueckner and K. M. Watson, *Nuclear Forces in Pseudoscalar Meson Theory*, *Phys. Rev.* **92** (1953) 1023–1035.
- [112] J. J. Sakurai, *Advanced quantum mechanics*. Pearson Education India, 1967.